**University of Nineveh**
**College of Electronics**
**Electronic Department**

# SIMULATION OF HIGH EFFICIENCY (InGaP/GaAs) SOLAR CELLS

**Marwah Maher Salem Al-Maola**

**A Master Thesis in**

**Electronic Engineering**

**Supervised by**

**Prof. Dr.**

**Khalid Khalil Mohammed**

**2021 A.D.**                                          **1443 A.H.**

# Simulation of high efficiency InGaP/GaAs solar cells

**A Thesis Submitted by**

**Marwah Maher Salim Al-Maola**

**To The Council of the College of**

**Electronics Engineering**

**University of Nineveh**

**As a partial Fulfillment of the requirements**
**For the Degree of Master of Science**
**In Electronic Engineering**

**Supervised by**

**Prof. Dr. Khalid Khalil Mohammed**

**2021 A.D.**                                      **1443 A.H.**

# ACKNOWLEDGEMENTS

## ABSTRACT

In present work, a tandem cell structure cell (InGaP/GaAs) is designed and simulated. This tandem cell consists of two cells, the first cell consists of indium gallium phosphide (InGaP) as an upper cell with an energy gap of 1.87 eV and the second cell consists of gallium arsenide (GaAs) as a lower cell with an energy gap of 1.42 eV and (GaAs) as a tunnel junction was simulated. The study is carried out using the specialized simulation program Silvaco Atlas, which is designed to simulate and study the behavior of semiconductor devices. The numerical modeling of the tandem cell efficiency design is simulated and the highest efficiency is obtained by varying some important parameters of the layers such as thickness and concentration of dopants in the multilayer cell as well as varying the tunnel junction material. The Silvaco software carried out the simulations and the results were achieved under spectrum AM1.5. To achieve this work: Firstly, the upper cell (InGaP) is designed and then the molar fraction of the indium content is changed to adjust the bandgap at 1.87 eV, and at this value, the highest solar efficiency was equal to 17.15%. Secondly, the bottom cell (GaAs) is designed and it was found that the efficiency after the simulation is 23.07%. Lastly, the two cells were stacked one on top of the other and connected by a tunnel junction of semiconductor material (GaAs). High operating factors for tandem cells are achieved by adding an Indium Aluminum Gallium Phosphide (InAlGaP) as a window layer with a bandgap of 2.3 eV and as a back-surface field (BSF) layer for the two cells, so the efficiency of the cell reached 25.10%. To improve the tandem cell design specification, the thickness of the BSF layer is studied and it is found that the performance of the solar cell was improved by increasing the thickness of this layer. The width of the BSF layer was optimized to give an efficiency of about 32.70% at a thickness of 2.1 μm, then the effects of doping concentration and the effects of the window layer thickness of the upper cell on the performance of the tandem cell

(InGaP/GaAs) were studied. The window layer thickness is changed from 0.01 μm to 0.06 μm. This change led to an increase in the efficiency from 32.70% to 33.59%. And the doping density of the window layer is also reduced from Na $=2\times10^{18}$ cm$^{-3}$ to Na$=1\times10^{18}$ cm$^{-3}$, which improved the efficiency and made it equal to 34.24%. Another improvement that has been applied to the tandem cell is changing the GaAs/GaAs tunnel junction material to InGaP/GaAs which leads to improving the overall performance of the cell and becomes equal to 34.39%. After obtaining the optimal tandem cell structure, the effect of temperature on optimal cell structure was investigated. It is observed that with increasing temperature from 300 K to 400 K in increments of about 25 degrees, the tandem cell efficiency reduces from 34.37 to 27.21 %.

# LIST OF CONTENTS

# LIST OF TABLES

## LIST OF FIGURES

# LIST OF ABBREVIATIONS

| ABBREVIATION | DESCRIPTION |
|---|---|
| a-Si | Amorphous silicon |
| AlGaAs / GaAs | Aluminum Gallium Arsenide / Gallium Arsenide |
| AlInGaP | Aluminum Indium Gallium Phosphide |
| AlGaAs | Aluminum  Gallium Arsenide |
| AlP | Aluminum Phosphate |
| AC | Alternating Current |
| Al | Aluminum |
| AM | Air Mass |
| AM0 | Air Mass Zero |
| AM1.5 | Standard terrestrial solar spectrum 'Air Mass 1.5' |
| B | Boron |
| BGN | band-gap narrowing model |
| BSF | Back surface field |
| CB | Conduction band |
| CdTe | Cadmium Telluride |
| CONMOB | standard concentration dependent mobility model |
| DC | Direct current |
| DJ | Dual Junction |
| $E_C$ | energy level of the conduction band |

| Abbreviation | Description |
|---|---|
| $E_V$ | energy level of the valence band |
| Eg | bandgap energy |
| EHP | electron hole pair |
| Eph | Photon Energy |
| EQE | External Quantum Efficiency |
| FF | Fill Factor |
| GaAs | Gallium Arsenide |
| Ge | Germanium |
| In | Indium |
| IR | Infrared |
| InP | Indium Phosphate |
| IQE | Internal Quantum Efficiency |
| InGaN | Indium Gallium Nitride |
| InAlP | Indium Aluminum Phosphate |
| InGaP | Indium Gallium Phosphide |
| InGaP/Si | Indium Gallium Phosphide / Silicon |
| InGaP / GaAs | Indium Gallium Phosphide / Gallium Arsenide |
| J-V | Current density – Voltage characteristics |
| $J_{SC}$ | Short circuit Current densities |

| Abbreviation | Description |
|:---:|:---|
| MPP | maximum power point |
| mun | mobility of electrons in Silvaco ATLAS |
| NREL | National Renewable Energy Laboratory |
| PV | photovoltaic |
| QE | Quantum Efficiency |
| $R(\lambda)$ | Reflectance |
| Si | Silicon |
| Sb | Antimony |
| SRH | Shockley-Read-Hall recombination  model |
| SILVACO | Silicon Valley Company |
| $T(\lambda)$ | Transmittance |
| TJ | Tunnel Junction |
| UV | Ultraviolet |
| $V_{OC}$ | Open Circuit Voltage |
| Vbi | Built in potential |
| VB | Valence Band |
| ZnO | Zinc Oxide |

# LIST OF SYMBOLS

| Symbol | Description |
|--------|-------------|
| A | Area |
| c | Speed of light |
| $G_p$ | hole generation rates |
| h | hole |
| $I_o$ | saturation current |
| $I_d$ | diode current |
| $I_{ph}$ | light generated current |
| $I_{sc}$ | Short circuit current |
| $I_{max}$ | max current |
| $I_{total}$ | total current |
| $III - IV - V$ | semiconductor compounds |
| $J_V$ | Recombinant current value |
| $J_P$ | hole current densities |
| $J_n$ | Electron current densities |
| k | Boltzmann constant |
| n | Electron concentration |
| $N_C$ | Conduction band effective density of states |
| $N_V$ | Valence band effective density of states |
| $N_d$ | Concentration of donor atom |

| Symbol | Description |
| --- | --- |
| $N_a$ | Concentration of acceptor atom |
| $p$ | Hole concentration |
| $P_{max}$ | Max power |
| $P_{out}$ | output power |
| $P_{in}$ | input power |
| $R_S$ | Series resistance |
| $R_{Sh}$ | Shunt resistance |
| $R_P$ | hole recombination rates |
| $T$ | Temperature |
| $v$ | Applied potential |
| $V_{max}$ | Max voltage |
| $\alpha$ | Absorption coefficient |
| $\varepsilon$ | permittivity |
| $\mu_n$ | Electron mobility |
| $\mu_h$ | Hole mobility |
| $\lambda$ | Wavelength |
| $h$ | Planck's constant |
| $\eta$ | Efficiency |
| $\rho$ | resistivity |
| $\sigma$ | conductivity |
| $a$ | lattice constant |

# CHAPTER ONE

# INTRODUCTION AND LITERATURE REVIEW

## 1.1 Introduction

In 1839, Edmund Becquerel detected that material combinations generate electricity if exposed to illumination. In 1877 Charles Fritts manufactured the first solar cell with the same structure as modernistic cells with an almost transparent thin gold layer of selenium covering. Nevertheless, its cells converted the recipient light energy to usable electrical current with an efficiency of less than 1% [1].

During the 1930s, little development was achieved in this field and solar cells have not been used as a possible source of power to provide electricity. However, in 1941 Russell Ohl first invented the first silicon solar cells, whose cell's performance was up to 6 percent in 1954 following developments achieved by Fuller, Chapin, and Pearson [2],[3].

After that, there have been many studies and researches in this field pertinent to photovoltaic cells, which has led to different kinds and generations of solar cells that can be categorized in general as three generations cells.

The first-generation of solar cells is also called photovoltaic silicon wafer. This technology is now dominating more than 85 percent of the solar cell market in the terrestrial application. These cells offer power conversion efficiencies up to 25%, although the fabrication technologies at present limit them to about 15 to 20% [4].

Materials of the second-generation are focused on the utilization of semiconductor deposits "thin-film" like the amorphous silicon (a-Si) and cadmium telluride (CdTe) Although thin-film cells of the second-generation usually have a lower efficiency (efficiencies around 6% to 10%) than silicon cells of first generation, the reduced manufacturing cost (watt per $cm^2$) has

been achieved. Furthermore, reduced mass allows panels to be fitted in light materials or flexible materials.

The primary objective of the solar cells of the third generation is not only to enhance the second generation solar cells' efficiency, but also to preserve the cost benefits. Several advances have been achieved in this field of investigation including dye-sensitized Nanocrystalline or Gratzel solar cells, photovoltaic organic polymer cells, multi-band photovoltaic, photovoltaic solar panels, and tandem (or multi-layer) solar cells. Among those all, in the past years, the multi-layer solar cell has become more and more interesting.

In order to more productively utilize the solar spectrum, solar radiation has become a widely dispersed resource, and several cells with various bandgap are linked in series to divide the wider spectrum into smaller parts, all of which could be more effectively converted to electrical energy [5]–[11]. It is the fundamental to discuss the concept of a multi-layer solar cell.

## 1.2 <u>Tandem cell structure and concept</u>

As seen in Fig. (1.1), the tandem cell (multi-layer cell junction) consists of (2 or 3) absorbers. The bandgap for each absorber varies from the other absorber in value.

To determine the performance efficiency of the tandem cells, the current-voltage characteristic (J-V) for the junction is significant. A total current is calculated by the total value of the short circuit ($J_{SC}$) and the recombinant current value ($J_V$).
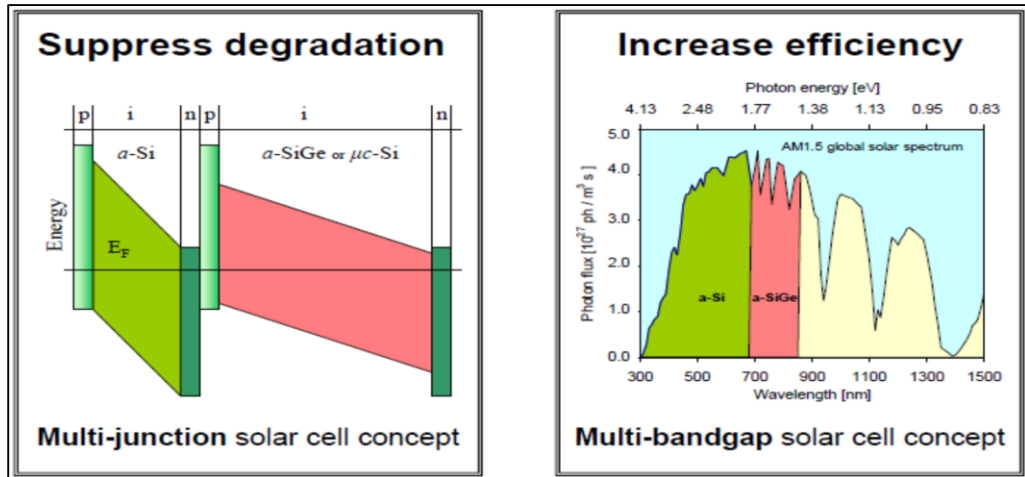
**Fig.(1.1)**   Illustrate the tandem solar cell's multi-layer as well as multi-band concept[12].

The tandem cells is produced typically when layers built up with the substrate material at the bottom of the cell on each other. The designer should also establish a tunneling contact between the various layers of the bandgap.

Typically the upper cell layer has the wider band gap, while the bottom layers has the lower band gap and operate with [lower energy photons], as illustrated in Fig. (1.2). Based on summing the charges produced in the top and lower cells, the total efficiency is determined [13].
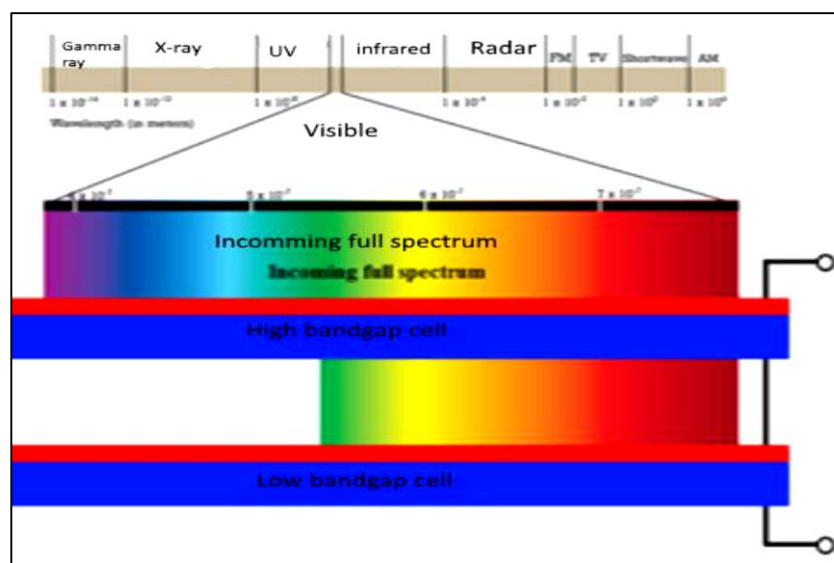


**Fig.(1.2)**   Depicts the spread of electromagnetic radiation for the spectrum via the tandem cell [12].

## 1.3 Literatures Review

In the mid-19th century, silicon cells were heart of the trade market[14]. However, the absorption loss is prominent due to the narrow light spectrum covered by this material. To overcome this problem, the solution is to use a tandem cell configurations. Jackson, E.D. [15] proposed the concept of multilayer cells. Wolf (1960) studied and researched tandem solar cells [16]. Fan, et al. (1982) performed tandem solar cells research based on computer analyses [17].

In the early years of photovoltaic cell technology (AlGaAs/GaAs), double junction solar cells, which were linked by tunnel diodes[18] and metal connections [19], have caused significant progress in this field. The manufacturing of the first tandem solar cell (AlGaAs/GaAs) in 1985 is achieved, by Hutchby, et al.

To demonstrate how the Silvaco ATLAS is used to simulate single layer and multilayer solar cells is based on materials of the compound III-V such as (Indium Gallium Phosphide), (Gallium Arsenide), and (Germanium), Michalopoulous has used tools available from the simulation program of Silvaco ATLAS[20].

The tandem cell (GaInP/Si) achieved an experimental efficiency of (9.9–10.4%) [21]. A semiconductor compounds with GaAs was already established and used for the solar cell space applications due to its higher radiation resistance and highly conversion efficiencies compared to Si cells [22].

In 2006, Lueck, et al. modeled the double junction solar cell InGaP/GaAs at a performance efficiency of 23.6% [23].

M. Fillali and B. Dennai also studied a GaInP/GaAs multilayer solar cells utilizing a heterojunction tunnel(p-InGaP/n-GaAs).Those researchers studies of various doping levels of the p-InGaP layer of the heterojunction tunnel, which permitted the optimal efficient structure under the

standardized conditions (AM1.5 and 300°K) to be achieved to a level of efficiency about 23.97 % ,$I_{SC}$ (mA) =1.501 , and $V_{OC}$ (V) =2.42097 [24].

Leem et al. created the InGaP/GaAs dual junction (DJ) solar cell in 2009 in order to optimize the current matching between the top and the bottom cells by utilizing a Silvaco ATLAS. The maximum current density $J_{SC}$ = 10.66 mA/cm$^2$, $V_{OC}$ = 2.34 V and FF = 87.84% were attained with the AM1.5G, showing a highest efficiency of 25.78% [25].

The National Renewable Energy Laboratory (NREL) has proved that GaInP/GaAs n-on-p tandems have a high efficiency (~27 percent terrestrial)[26].

Also under normalized conditions (1sun) with the AM1.5G spectrum, S.R. Kurtz, and others achieved an efficiency of 27.3% with (Ga0.5In0.5P/GaAs) structure. The $J_{SC}$ = 13.6 mA/cm$^2$, FF = 87 % ,and $V_{OC}$ = 2.29 V are included in that tandem cell [27].

In 2018, K. K. Mohammed achieved an efficiency of (29.98%), by designing a tandem cell with a thickness of about 0.7 μm regarding to the top (InGaP) cell and about 2.8 μm regarding to the bottom cell (GaAs). Values for this tandem cell included: $J_{sc}$ = 29.21 mA/cm$^2$, FF = 75.6% and $V_{OC}$ is (1.356 V)[12].

M. Benaicha, et al. in 2020 have designed and analyzed monolithic multi-junction (MMJ) structures by using (GaAs) tunnel diode. The results at this tandem cell were inclusive for $V_{OC}$ =2.07 V, $J_{SC}$ =17.04 mA/cm$^2$, FF =87.99 %, and η =31.11 % under AM 1.5 spectral conditions [28].

Michael H. Tsutagawa and Sherif Michael accomplished an efficiency of 32.593% by using "Genetic Algorithm Design Parameters" in the simulations of the dual junction solar cell (DJ). This cell's structure included these values $V_{OC}$ = 2.483 V, $J_{SC}$ = 19.853 mA/cm$^2$, and FF = 89.473 % that was achieved at the condition of AM0 illumination[29].

## 1.4 <u>Aim of the work</u>

The aim of the present work is design and simulate a multilayer solar cell (tandem). The optimum cell structure has been found after studying the effect of changing the materials, thickness, and doping level on the performance of the tandem cell.

## 1.5 <u>Organization of the thesis</u>

The thesis consists of five chapters:

Chapter one contains an introduction about solar cells and describes the concept of multilayer solar cells.

Chapter two includes the fundamentals of solar cells and semiconductor materials.

Chapter three explains the Silvaco ATLAS software and the steps utilized for modeling the tandem cell.

Chapter four addresses with the results of the simulation of the tandem cell.

And lastly, Chapter five discusses the conclusions and the future works in this field.

# CHAPTER TWO

# SEMICONDUCTOR AND SOLAR CELL FUNDAMENTALS

## 2.1 Generation rate and recombination

The method of generating and recombining electron-hole pairs inside a semiconductor is explained by B.G. Streetman and S.K. Banerjee[30]. Material absorbing photons have an energy greater than the bandgap while balanced via direct or indirect recombination. Fig. (2.1) shows this phenomenon more simply. It is worth observing that the energy of the light or a photon that is entering the material should be higher than the bandgap energy which generates electron-hole pairs (EHP) in the current material. This process also occurs with similar energies which can penetrate the material and influence the material's bandgap.
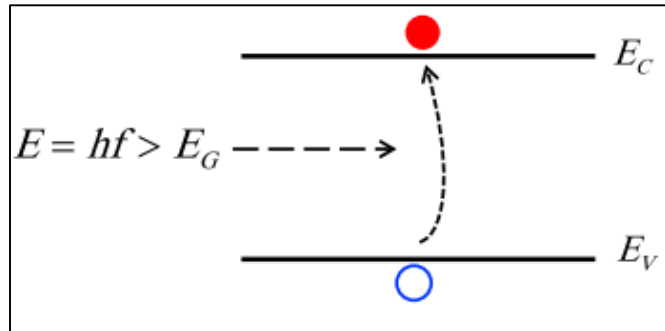


**Fig.(2.1)** Light generating electron-hole pairs [31].

In carriers continuity equation about semiconductor, the Drift-Diffusion, generation, and recombination are synchronizly analyzed as shown in the next equations[32]:

$$\frac{\partial n}{\partial t} = \frac{1}{q} \, div \vec{J}_n + G_n - R_n \qquad (2.1)$$

$$\frac{\partial p}{\partial t} = -\frac{1}{q} \, div \vec{J}_p + G_p - R_p \qquad (2.2)$$

Where $J_n$, and $J_P$ are the electron and the hole current densities, $G_n$, and $G_P$ represent the generation rates of electron and hole, while $R_n$, and $R_P$ represent the recombination rates for electron and hole respectively. The electron charge is represented by (q). The current densities are expressed in drift- diffusion model as follows[32]:

$$\overrightarrow{J_n} = q\mu_n \, \boldsymbol{n}\boldsymbol{E} + qD_n \nabla n(x) \qquad\qquad (2.3)$$

$$\overrightarrow{J_P} = q\mu_p pE + qD_p \boldsymbol{\nabla}\boldsymbol{p}\,(\boldsymbol{x}) \qquad\qquad (2.4)$$

## 2.2 The fundamentals of solar cells

Following the completion of the fundamentals of semicondutors, it is logical to explain the basics of solar cells.

### 2.2.1 The electromagnetic spectrum

The electromagnetic spectrum is a "Light consists in the transverse undulations of the same medium which is the cause of electric and magnetic phenomena" (James Maxwell)[33]. The usable part of this spectrum for power generation is the ultraviolet (UV), the visible, and the infrared (IR) wavelengths. The total electromagnetic spectrum is shown in Fig. (2.2).
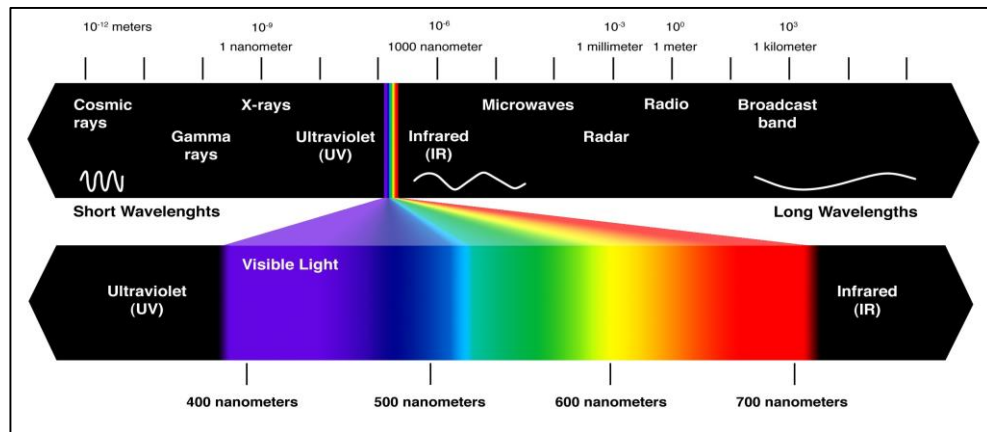


**Fig.(2.2)** An overview of the total spectrum of light[34].

As mentioned above, the Light consists of photons. The energy of the photons is depends on the wavelength.

A visible range starts from wavelength 390 nm to 780 nm. Solar irradiance has the biggest magnitude at the visible wavelengths and its peaks are at the blue and green lights[20]. Table (2.1) displays the range of the approximate wavelength of different colors of the visible spectrum in a vacuum.

**Table (2.1)**   Approximate wavelength of various colors in vacuum[35].

| Color | Wavelength (nm) |
|-------|-----------------|
| Red | 780-622 |
| orange | 622-597 |
| Yellow | 597-577 |
| Green | 577-492 |
| Blue | 492-455 |
| Violet | 455-390 |

## 2.2.2 Photovoltaic effect

A solar or photovoltaic (PV) cell is a semiconductor device, which transforms photons directly into electric current and voltage. The sun itself is the principal source of the photons. The structure of a photovoltaic cell can be better understood from Fig. (2.3).

The PV influence in a solar cell can be explained in 3 stages[36]:

- Generation of additional carriers due to Light's Absorption.
- The separation of charge carriers (positive and negative).
- Extraction of the charge carriers in the external circuit.
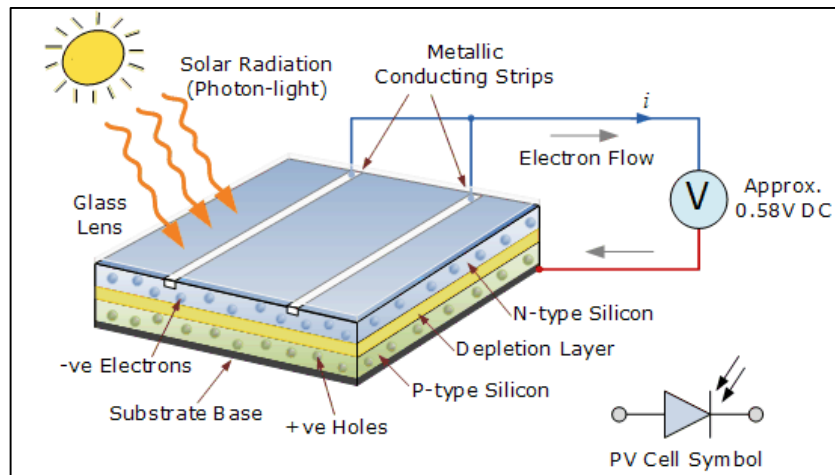
**Fig.(2.3)** Cross section of photovoltaic cell[37].

When the light is absorbed by the material, for example, semiconductor, the photons provide electrons with the energy to move into higher energy levels in materials. The excited electrons, nevertheless, returns to their original state of energy. This makes it possible to pass the excited electrons to an external circuit before returning to their original energy status.

## 2.2.3 Light absorption

All semiconductor materials have an inherent feature to absorb various wavelengths of light that are measured by the absorption coefficient they have. The absorption coefficient measures the distance at which a particular wavelength of light can permeate the material before it is absorbed.

The absorption coefficient depends on the incident light's wave length and dielectric material[38]. Fig. (2.4) shows the absorption coefficients of semiconductor materials that are widely used in photovoltaic applications.
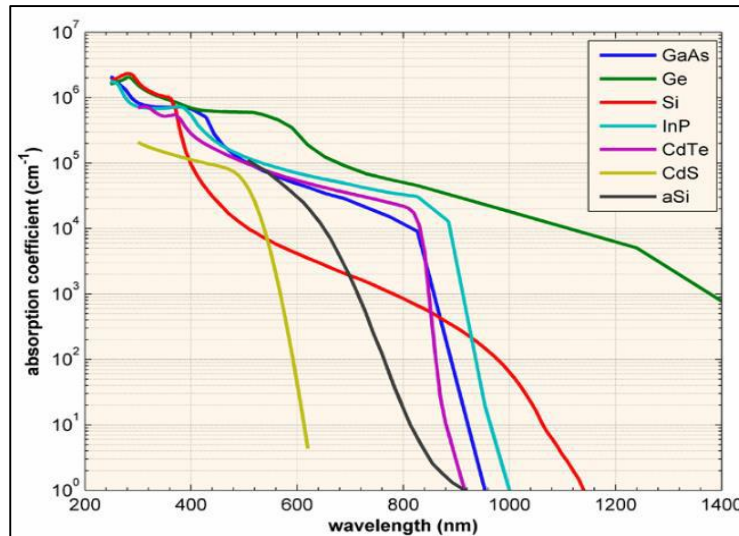
**Fig.(2.4)** Absorption coefficients of widely used semiconductor materials[38].

Scientists and researchers use the absorption coefficient values of the semiconductor materials in order to determine the optimum thickness of the solar cells that combine two or more semiconductor materials with various band gaps and various absorption coefficients.

## 2.2.4 Principle work of the solar cells

First of all, a solar cell can be defined as a simple p-n junction or diode. The top of the semiconductor solar cells is an n-type material, this n-type material behaves as the emitter, while the p-type material is the base or the substrate[39] as Fig. (2.5) demonstrates.
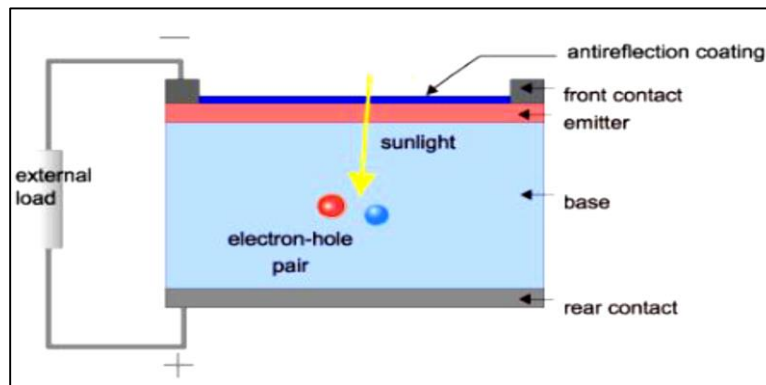


**Fig.(2.5)** The Simple structure of the solar cell[32].

Solar cells produce electricity by using the energy stored in light photons to create pairs of electron-hole (EHP). These charge carriers diffuse in the solar cell structure. The p-n junction separates charge carriers with the assist of an electric field created in the depletion region due to ionized dopant atoms[32].This separation assists and enables carriers to be collected in contacts before the recombination occurs. Fig (2.6) displays the principle of a simple solar cell.
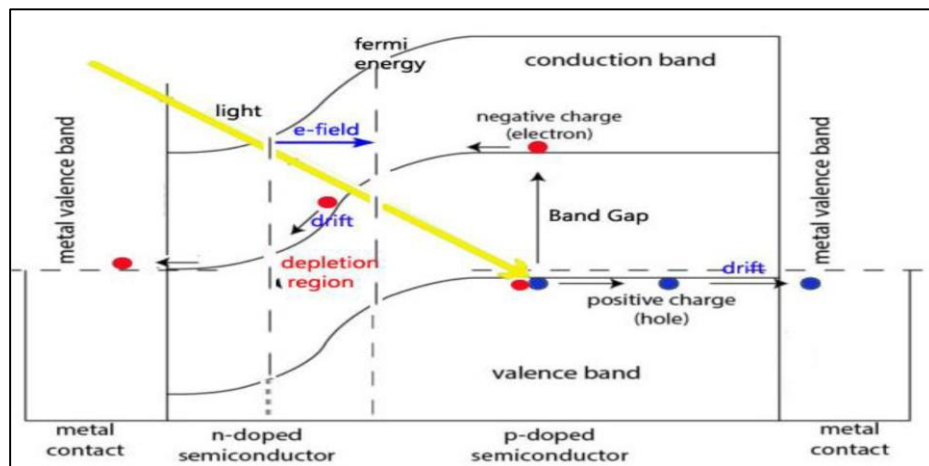


**Fig.(2.6)** The working principle of solar cells[38].

## 2.2.5 Solar Cell Performance

There are important parameters that must be computed carefully in order to understand the principle solar cell which are:

- Short circuit current ($J_{SC}$).
- Open-circuit voltage ($V_{OC}$).
- Fill factor (FF).
- Efficiency ($\eta$).

$J_{SC}$ and $V_{OC}$ are required in order to draw the J-V solar cell curve for determining the maximum power point ($M_{PP}$).

Fig. (2.7) illustrates the equivalent solar cell circuits in the darkness and in illumination[40],[41].
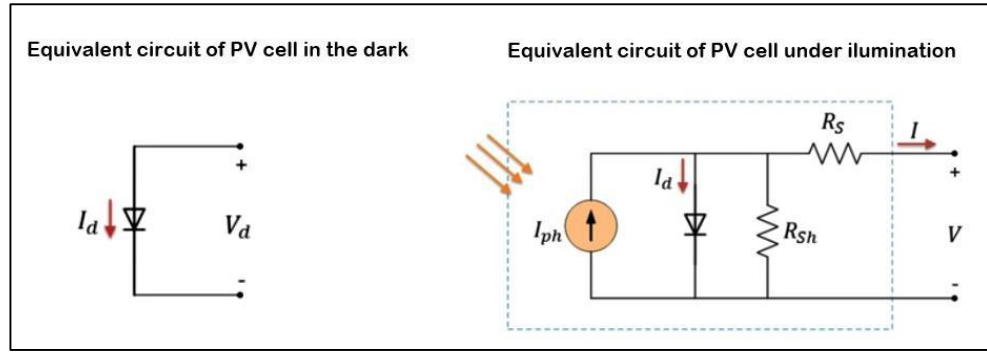
**Fig.(2.7)** Equivalent circuit of solar cells[38].

$I_d$ matches to the diode current; $I_{ph}$ is the generated current by the solar cell illumination, based on intensity radiance solar. $R_S$ represents the series resistance that demonstrates the inner electric losses. $R_{sh}$ is the parasitic shunting resistance cell due to some drawbacks in the solar cell.

a. **Short circuit current ($I_{SC}$)**

It is a significant parameter. Whenever the load resistance $R_L$ is equal to zero, the voltage is also zero[42], resulting in a short circuit current.

It is the difference amidst the total current ($I_{total}$) produced by the photon and the current that is generated by the diode in the dark as shown in eq. (2.5). $I_{SC}$'s flow comes from light-generated charge carrier's collecting and generating it depends essentially on the quantity of the incident photons of their spectrum, the area of the solar cell, and the optical properties. The $I_{SC}$ is explained by the eq. (2.6)[43]. Short circuit current density ($J_{SC}$) and its unit (mA/cm$^2$)[44]are shown in eq. (2.7)[38].

$$I_{total} = I_0 \left( e^{\frac{qv}{nKT}} - 1 \right) - I_{ph} \qquad (2.5)$$

$$I_{SC} = -I_{ph} \qquad (2.6)$$

$$J_{SC} = \frac{I_{sc}}{A} \qquad (2.7)$$

Where q is the electronic charge, v is the voltage applied across the p-n junction, $n$ is the ideality factor, K is Boltzmann's constant, ($I_0$) is the darkness current or (saturation current), $J_{SC}$ is Short circuit current density and T is temperature and its unit kelvin (K).

## b. Open circuit voltage ($V_{OC}$)

The solar cell terminals' maximum voltage in the case of no load is connected with the solar cell, i.e. ($I = 0$) as shown in eq. (2.8).

$V_{OC}$ is obtained in the unit mV or V [44].

$$V_{OC} = \frac{nKT}{q}\ln\left(\frac{Iph}{I0} + 1\right) \qquad (2.8)$$

The equation above shows that ($V_{OC}$) depends on $I_0$, and $I_{ph}$. $I_0$ is dependent on the recombination in the solar cell; therefore $V_{OC}$ is considered a measure of the amount of recombination in a solar cell. Fig. (2.8) shows the graphic representation of the open-circuit voltage.
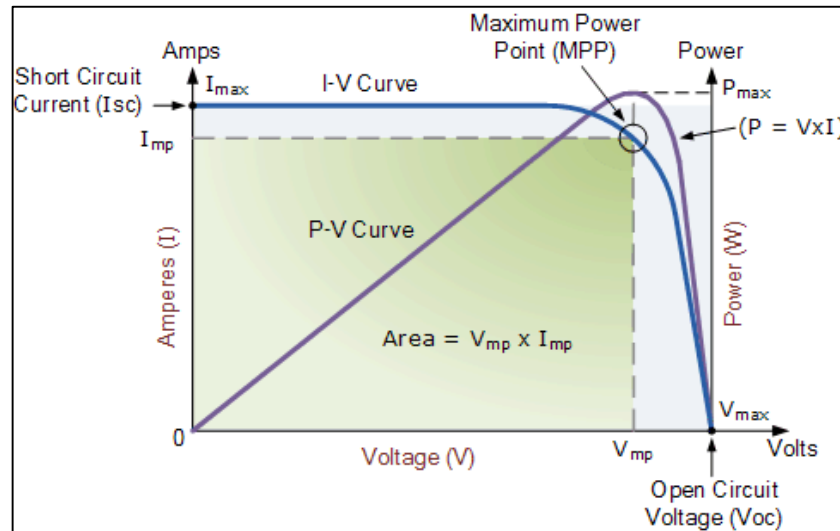


**Fig.(2.8)** The representation of $I_{SC}$ and $V_{OC}$ in the I-V curve[38].

## c. **Fill Factor (FF)**

Fill factor (FF) is the ratio of the maximum theoretically attainable power to the actual maximum achievable power in the solar cell. The fill factor is the biggest possible area, which a rectangle may fit under the I-V curve[45]. eq. (2.9) shows how to obtain the fill factor of a solar cell[46]. In the ideal case of solar cells, it is preferred to have a fill factor of 1.

$$FF = \frac{V_{max}I_{max}}{Voc\ Isc} = \frac{Mpp}{Voc\ Isc} \qquad (2.9)$$

Where $M_{pp}$ is the maximum power point, $I_{mp}$ is the maximum current point, and $V_{mp}$ is the maximum voltage point. Fig. (2.8) displays an I-V characteristic for the solar cell together with a maximum rectangle, in addition to the maximum power point ($M_{pp}$) of the solar cell.

## d. The maximum efficiency (η)

The efficiency (η) of a solar cell is generally expressed as the ratio of the output power ($P_{out}$) to the input power ($P_{in}$) as shown in eq. (2.10)[44]. It is also shown in form of a percentage.

$$\eta_{max} = \frac{P_{out}}{P_{in}} = \frac{V_{max}I_{max}}{P_{in}} \qquad (2.10)$$

The solar cell output power ($P_{out}$) is calculated by eq. (2.11)[37] and given in watts.

$$P_{out} = V_{out} I_{out} \qquad (2.11)$$

The solar cell will supply maximum power at the maximum values of voltage ($V_{mp}$) and maximum current ($I_{mp}$) as illustrated in eq. (2.12)[46]:

$$P_{max} = V_{max} I_{max} \qquad (2.12)$$

In terms of fill factor maximum power is by putting eq. (2.9) in eq. (2.12) we get[37]:

$$P_{max} = V_{OC} I_{SC} FF \qquad (2.13)$$

Therefore, the mathematical expression of the efficiency derived from eq. (2.10) and eq. (2.13) is[37]:

$$\eta = \frac{V_{oc} I_{sc} FF}{P_{in}} \qquad (2.14)$$

Where $P_{in}$ represents the incident solar radiation. The $P_{in}$ depends on the number of the air mass, which is related to sun location. As shown in Fig. (2.9), the atmosphere path at whatever zenith angle (Θ) is directly related to the air mass (AM)
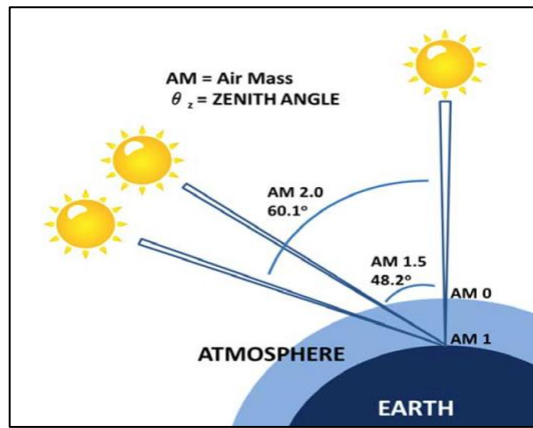
**Fig.(2.9)** The atmospheric path length in air mass (AM) units varies with zenith angle (Ө)[47].

The approximate atmosphere path length can be equal to 1/cos Ө as shown in eq. (2.15), where Ө is the angle between the sun and the point directly overhead[47], so:

$$AM = \frac{1}{\cos\theta} \qquad\qquad (2.15)$$

Fig. (2.10) displays the solar irradiation spectrum for two air-mass (*AM*) conditions.
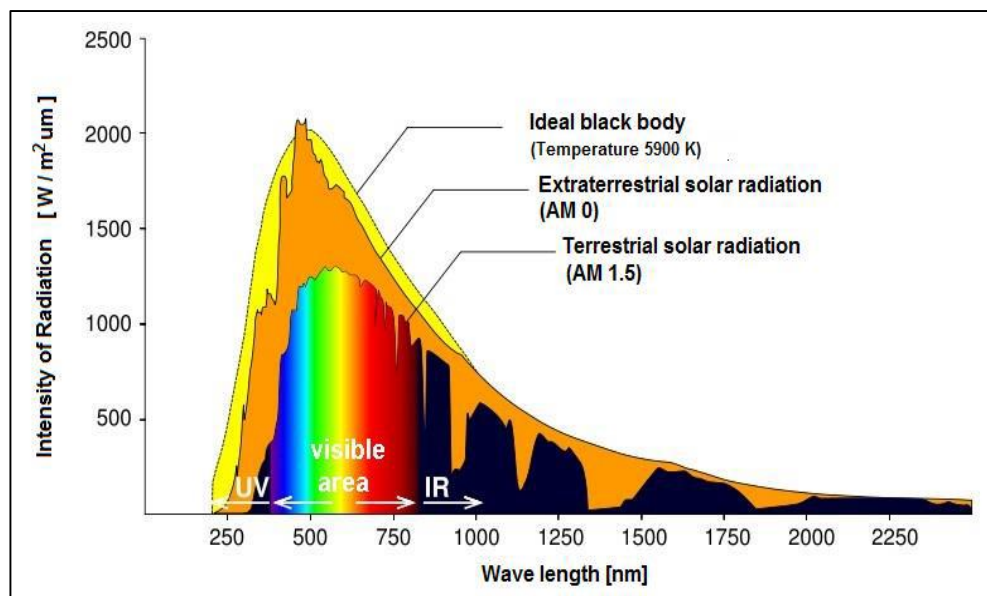


**Fig.(2.10)** Solar irradiance spectrums versus wavelength[42].

The top curve is the solar irradiance spectrum called the Air Mass Zero (AM0) and is measured outside the earth's atmosphere. Under *(AM0)* condition, the intensity irradiant power of the sun is 136.61 $mW/cm^2$ or 1360 $W/m^2$. (AM0) is used in space applications. The bottom curve is the AM1.5's which is the standard spectrum on the surface of the earth, and it is most commonly used for terrestrial applications to calculate the solar cell efficiency. Specifying the accurate (*AM*) condition is so important[42]. Under *AM*1.5 conditions, the intensity irradiant power of the sun is $100 mW/cm^2$ when the sun is at a zenith angle equal to ($\theta = 48.2°$).

**e. The Series Resistance (R$_S$)**

Charge carriers that are created and separated in the cell structure, passes through the semiconductor materials, the semiconductor metal interface, and metal areas one after another that facade up with resistance in each area. The total resistance along this path is referred to as series resistance (R$_S$). Emitter region and base region in particular, front contact and back contact ,slices, bus bars, and wafer edges participates in series resistance value, and eq. (2.16) can be stated as follows[48]:

$$R_S = R_e + R_b + R_{front} + R_{back} + R_{bus} + R_{sl} + R_{edge} \qquad (2.16)$$

Where is emitter resistance, $R_b$ is base resistance, $R_{front}$ is front contact resistance, $R_{back}$ is back contact resistance, $R_{sl}$ is slices resistance, $R_{bus}$ is bus bars resistance , $R_{edge}$ wafer edges resistance.

For a proper solar cell, the series resistance (R$_s$) must be kept as small as feasible. The series resistance value can be computed numerically via taking the derivative of the I-V characteristics curve at the point V = V$_{OC}$. The influence of series resistance (R$_S$) on the solar cell diode equation can be seen in the following eq. (2.17)[49]:

$$I = I_{\text{ph}} - I_0 \left( e^{\frac{qV + IR_S}{kT}} - 1 \right) \tag{2.17}$$

The influence of the series resistance ($R_S$) on the I-V characteristics curve is clear in Fig. (2.11(a)) on the left side. This figure illustrates that rising series resistance ($R_{S)}$ has a negative effect on the I-V characteristics curve[50].
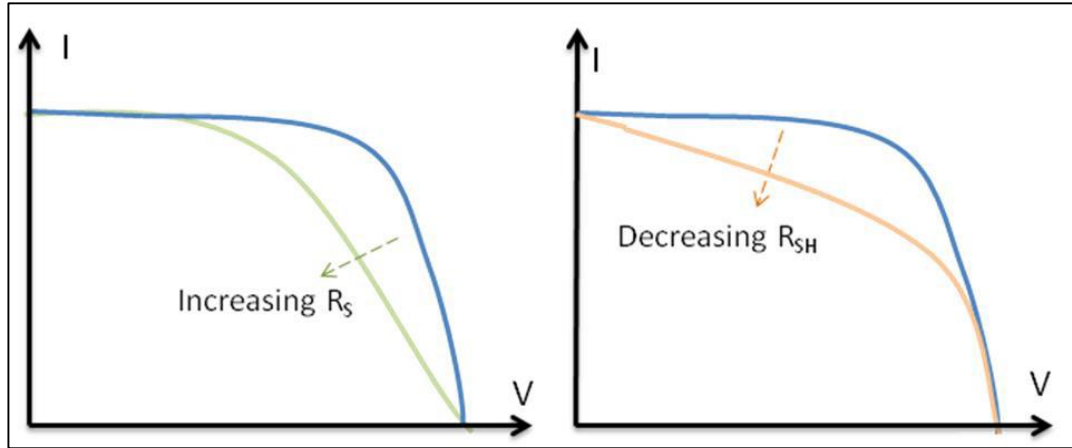


**Fig.(2.11)** (**a**). The effect of the series resistance (**b**). The effect of the shunt resistance[50].

### f.   **The shunt resistance ($R_{SH}$)**

The resistance value among positive and negative contacts is called shunt resistance. For a succeeded cell, it is anticipated to be quite large, otherwise, there is an unwanted alternate path for carriers to complete the circuit. Manufacturing defects are the possible explanation for less shunt resistance. Edge isolation is one of the key techniques in the prevention of edge leaks to increase shunt resistance.

The shunting resistance may be measured using the I-V characteristics curve derivative at the point V = 0, and the influence of the shunt resistance may be noticed on the solar cell diode eq. (2.18)[49]:

$$I = I_L - I_0 \left( e^{\frac{qV}{kT}} - 1 \right) - \frac{V}{R_{Sh}} \tag{2.18}$$

Shunt resistance ($R_{sh}$) can be utilized as a pointer of the leakage current in the solar cell device. High shunt resistance ($R_{sh}$) means that the

current leakage level is low, which for the solar cell system is desirable. The influence of the shunt resistance ($R_{sh}$) on the I-V characteristics curve of a solar cell is shown in Fig. (2.11) (b) on the right side. This figure illustrates that shunt resistance ($R_{sh}$) decreasing has a negative influence on the I-V characteristics curve and subsequently on the maximum solar cell power[50].

**g. Quantum efficiency (QE)**

The quantum efficiency QE is the number of free charge carriers that are generated and collected by the solar cell divided by the number of incident photons[51].

The QE is given as a function of wavelength or as energy. In other terms, the QE is closely related to the solar cell's spectral response to various wavelengths. If all photons of a specific wavelength are absorbed and the resulting minority charge carriers are collected, so the quantum efficiency at that specific wavelength is1. For photons with energy below the band gap, the quantum efficiency is 0.

QE can be assessed in several ways, for example, as External Quantum Efficiency (EQE) or Internal Quantum Efficiency (IQE). The EQE is the ratio of the number of electron-hole pairs (EHP) collected to the number of incident photons on the illuminated cell. Fig. (2.12) display the quantum efficiency QE for a silicon solar cell. EQE is given at a certain wavelength λ as shown the following eq. (2.19)[52].

$$EQE\ (\lambda) = \frac{Jsc\ (\lambda)}{q\varphi\ (\lambda)} \qquad (2.19)$$
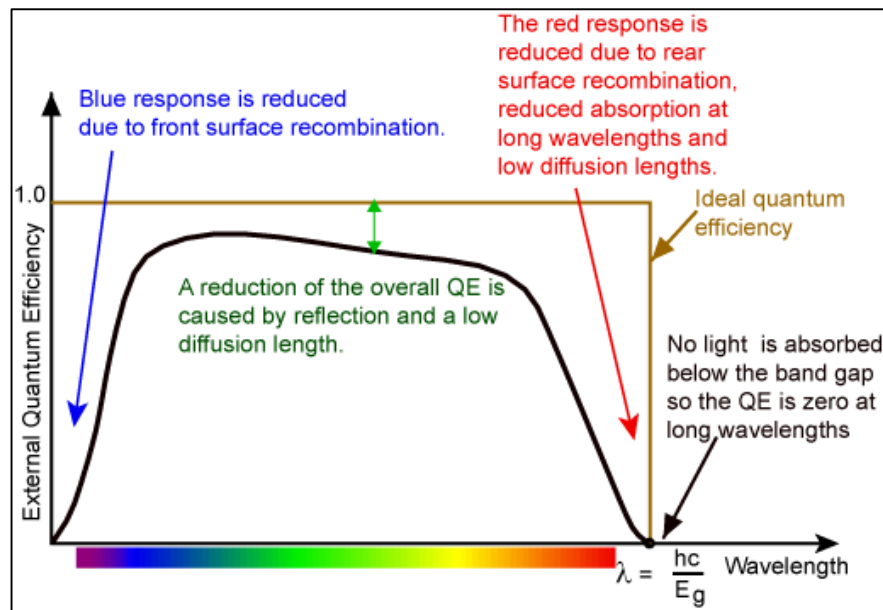
**Fig.(2.12)** The quantum efficiency QE for the silicon solar cell[53].

Where: $J_{SC}$ ($\lambda$) is the short-circuit current density and $\Phi$ ($\lambda$) is the photon flux; q is the charge of an electron.

Internal quantum efficiency (IQE) refers to the quantum efficiency, which can be generated by photons that did not reflect or transmit from the cell. Mathematically, the IQE may be determined by using the EQE as shown in eq. (2.20)[52].

$$IQE = \frac{EQE\ (\lambda)}{1 - R\ (\lambda) - T\ (\lambda)} \qquad (2.20)$$

Where: R ($\lambda$) is the reflectance of the cell, T ($\lambda$) is the transmittance of the cell.

### 2.2.6 Multi-layer solar cells

A traditional single-layer solar cell has a distinctive band gap (Eg). The semiconductor materials band gap usually determines how the photovoltaic cell responds to light and determines the light's wavelength, which meets generating the electrical energy requirements. The relation between band gap (Eg) and wavelength ($\lambda$) is described in eq. (2.21)[54].

$$\lambda \leq \frac{h\,c}{\text{Eg}} \qquad\qquad (2.21)$$

$$\lambda(\mu m) \leq \frac{1.24}{\text{Eg}}$$

Where (Eg) in eV, $c$ is the speed of light in meters per second, ($h$) is the Planck's constant, and ($\lambda$) is the photon's wavelength in micrometers. For example, In Gallium Arsenide (GaAs), the wavelength that agrees to 1.42 eV is 0.873 $\mu$m.  The maximum photocurrent extracted from a solar cell can be determined through this band gap (Eg) of the semiconductor materials, when a photon has energy ($E_{ph}$) that occurs at the p-n junction. The photons that have an energy ($E_{ph}$), greater than this band gap (Eg) are efficiently absorbed. The extra energy is dissipated through a process known as thermalization by transmitting heat to the crystalline lattice. If ($E_{ph}$) is smaller than (Eg), however, the junction does not absorb the photon and hence does not collect its energy. The efficiency of a single-junction solar cell in general is inherently limited. Fig. (2.13)  shows the efficiency as a function of the band gap.
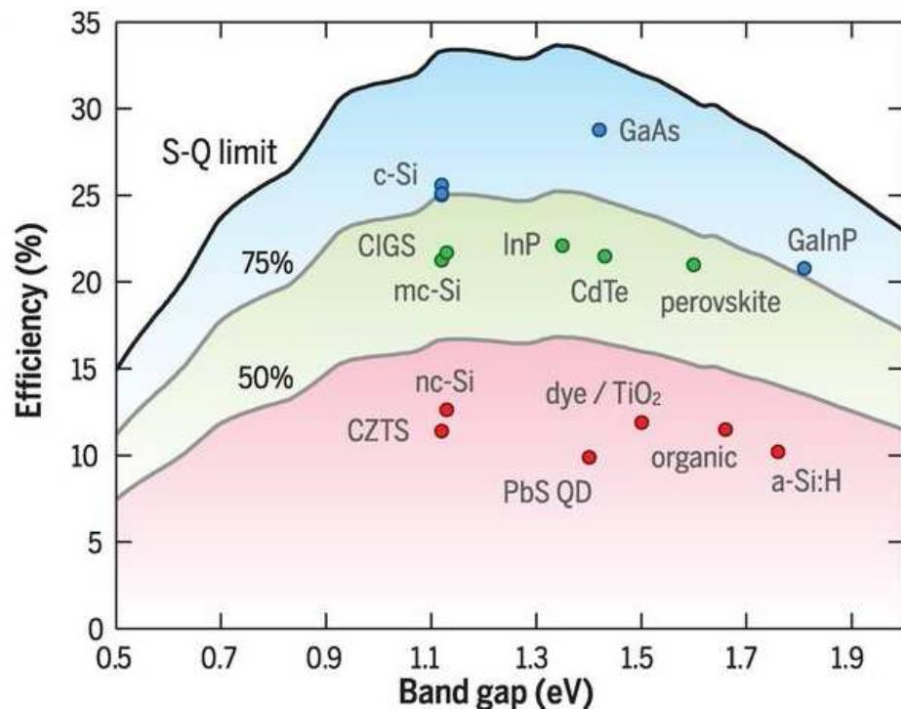
**Fig.(2.13)** The efficiency border as a function of bandgap[55].

One approach to circumvent this constraint conceptually is by dividing the spectrum into numerous spectral areas and converting each area into a separate junction. Each layer has various bandgaps. Therefore, each layer thus absorbs and transforms photons having energy larger than its layer's bandgap and less than the higher layer's bandgap[56]. (See Fig. (2.14) left illustration). The materials' bandgap is less and smaller from top to bottom. This process is known as spectrum separation. That means the solution is to fabricate multi-layer solar cells. Stacking single-layer solar cells in series creates a larger area for energy generation. This design extends the solar spectrum range to increase absorption and decrease thermal loss [41]. The higher cost of multi-layer solar cells limit their use to highly specific applications, including space applications. Fig. (2.14) displays, a highly doped, thin tunnel junction is putted between sequential p-n junction layers to decrease the forward bias voltage drop from the simple p-n junction.
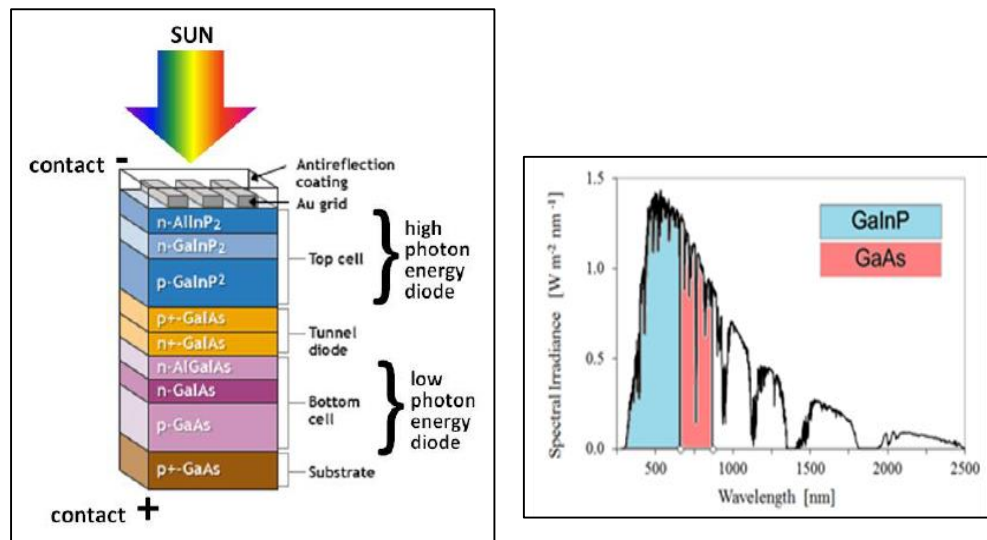
**Fig.(2.14)** Typical buildup of high-performance solar cell with Multi-Junction Solar Cell (tandem) structure vs. Solar Spectrum[57].

## 2.2.7 The manufacturing of Multi-layer solar cell

The stacking of solar cells is done through one of two methods[58]:

1. They can indeed be mechanically stacked by placed one complete cell on top of another. Because metallization existences between the cells so they are really linked in parallel. Thus, eliminating the current constraints in the tandem cell. This method is very costly and hard for except for some trial cells to be established.

2. The stacking of individual p-n junctions a top each other in series to create a multi-layer device. This mechanical stacking is called a tandem cell. Although this procedure is significantly harder and more expensive than manufacturing a single junction solar cell, its cost is affordable for space applications. The quantum efficiency is an illustration of how efficiently every junction in a tandem cell absorbs a certain portion of the spectrum of light. Figure (2.15) illustrates the quantum efficiency of the modeled solar cell. In an ideal case, these will be two distinct curves and not overlapped.
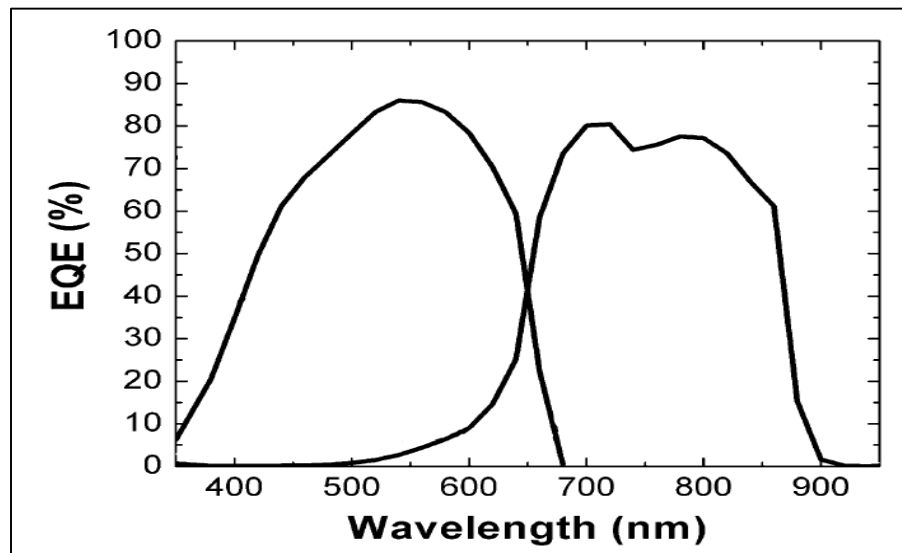
**Fig.(2.15)** (EQE) of the dual-junction solar cell[58].

In this tandem cell (dual-junction), carrier generation operates precisely like in a single-layer solar cell. Nevertheless, the location of charge carriers  generated, is becomes more important. The cells are linked in series in the dual-junction configuration are and the current is limited to the smallest current produced in the series. Both cells in the tandem cell must produce about the same quantity of current to minimize wasted current. The highest bandgap semiconductor material in the dual-junction or tandem cell must be positioned at the top, to allow to absorbing just the photons of the highest energy and permitting all of the low energy photons to pass into lower cells to participate in the photo- generation rate in these lower cells. In Fig. (2.15), the curve on the left describes the top junction with the peak absorption of a top junction at a shorter wavelength and the highest energy. The component cells that are serially connected might limit the current. Yet, in the tandem cell, increases substantially the voltage at which the cell functions.Theoretically, this kind of dual–junction (tandem) looks like the cell shown in Fig. (2.16) but the problem is substantial, since stacking a p-n junction on top of the other produces a parasitic p-n junction between the two cells. This parasitic junction provides an electro field in the opposite direction of fields generated via the component cells and caused

unacceptable electric losses inside the cell because of opposite current motion. Fortunately, a special type of p-n junction, called a tunnel junction, can be inserted between the cells to alleviate this issue.
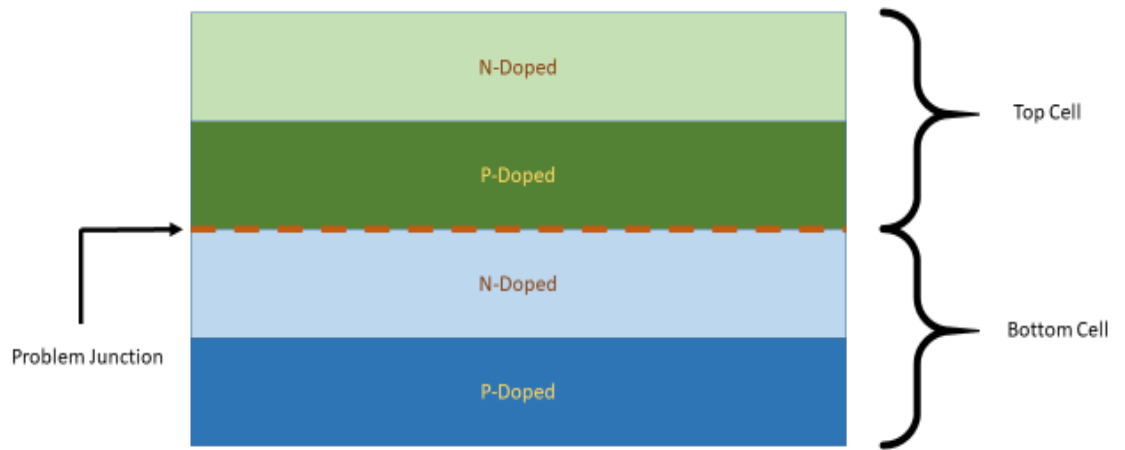


**Fig.(2.16)** Tandem Cell without Tunnel Junction[58].

## 2.2.8 Tunnel Junctions in Multi-layer solar cell

A serial electric connection of the sub cells is necessary for the multi-layer solar cell. The tunneling diode is put into an inverse polarization among the two cells. The tunnel junction(TJ) with a bigger band gap is necessary to improve the properties of the solar cell[59]. A tunnel junction takes place when a p-n junction has been quite heavily doped that it stops operating as a conventional diode. Less optic and electrical loss must be used in links; this is why the best choice is to build a tunnel intersection with a high impurity concentration[44], and if the tunneling junction is doped lower, the cell will be influenced by lower temperature

The tunneling case happens when the two sides of the junction become degenerate, meaning the Fermi levels are inside the valence and conductions bands themselves [60]. Complete comprehension of Fermi levels and band physics throughout a junction is so important to totally comprehend the principles of how a tunnel diode works.

The current-voltage characteristics of a tunnel junction are shown in figure (2.17). When this diode is reverse biased, it does not completely block current, however, it operates instead as a resistor. Thus, when properly biased, current can pass through in the opposite direction of a normal diode[60].
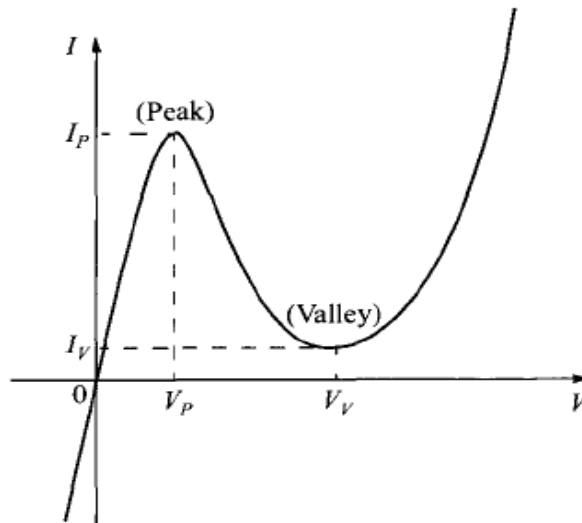


**Fig.(2.17)** Tunnel Junction Current Voltage Relationship[60].

This permits such a p-n junction to be put among two cells in the tandem cell in the opposite direction of the component p-n junctions without damaging the current of the total cell. This removes the accidental creation for conventional p-n junction in the reverse direction, as seen in Fig. (2.18). The tunnel junction can be modeled as a defect path between the BSF layer of the upper cell and the window layer of the lower cell[61].

**Fig.(2.18)** Tandem Solar Cell with Tunnel Junction[58].

## 2.2.9 Materials compatibility in Multi-layer solar cell

Semiconductors are 3-D shaped in their cell. The unit cell's construction assists to clarify the idea of the lattice as is explained in Fig. (2.19).



**Fig.(2.19)** The unit cell lattice structure[20].

The letter "a" is displayed on each edge of the cube in Fig. (2.19). The symbol "a" is the lattice constant. Each material of the semiconductors materials has a lattice constant. So when staking crystals of different semiconductors materials on top of each other (multi-junction solar cells), the lattice constants of the materials should be matched. In certain cases, it can be possible to develop a window layer on the top of the cell to embank

several material variations, and for avoiding recombination and increasing the short circuit current. Also adding the back surface field (BSF) layer is necessary[62]. The BSF-layer that placed after every p-n junction layer leads to confinement and efficiency in collecting minority charge carriers and generally has a wide bandgap[63]. The selection of layers for a multi-layer solar cell must thus be made depending on both compatibilities of materials (lattice-matched) and performance standards. Fig (2.20) displays the bandgap and lattices constants for the III–V elements like P, As, Sb, and N alloys.
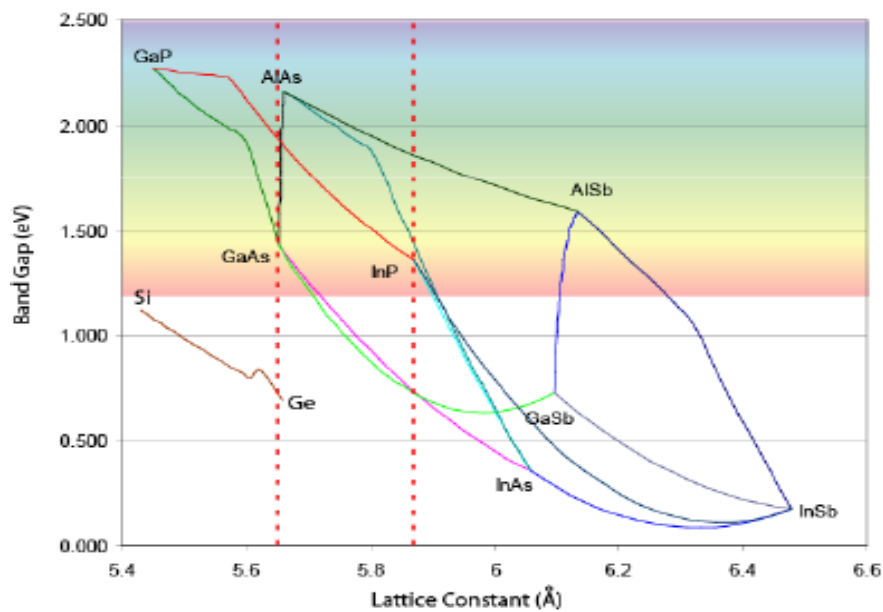


**Fig.(2.20)** Bandgap energy and lattice constant for different material compound[24].

The following example demonstrates the lattice matching of (InGaP to GaAs). InGaP is an alloy made up of (x) parts Gallium Phosphide (GaP) and (1-x) parts Indium Phosphide (InP). As a result, Indium Gallium Phosphide (InGaP) is denoted as $In_{1-x}Ga_xP$.

The lattice constant of GaAs   α=5.65Å, InP has α=5.87Å, GaP has α=5.45Å.

The equation for calculating (x) is[20]:

$$a_{GaAs} = a_{GaP} . x + a_{InP} . (1 - x) \Leftrightarrow x = \frac{a_{GaAs} - a_{InP}}{a_{GaP} - a_{InP}} \quad (2.22)$$

If x=0.49 (In$_{0.49}$Ga$_{0.51}$P), where GaP has Eg=2.35 eV and the InP has Eg=1.35 eV therefore, In this instance, the bandgap is[20]:

$$E_g^{GaInP} = x . E_g^{GaP} + (1-x) . E_g^{InP} \qquad (2.23)$$

Which gives Eg = 1.87 eV .As a result, a double-junction solar cell with InGaP at 1.87 eV and GaAs at 1.42 eV can be constructed.

## 2.2.10 The electrical Limitations

A multilayer solar cell seems a lot like multiple different batteries that are connected in series when generating energy. The voltage and current rates for each battery are various for a given electric load, when the batteries connected in series. Their total power producing is determined by the subsequent equation (2.22)[64].

$$P_{total} = I_{load} \ \Sigma V_{junctions} \qquad (2.24)$$

With the increasing number of connecting layers (junctions), the load current becomes a more difficult design concern. To use the maximum output power from the junction layer, load current should be near to the maximum power point current of the junction layers. Usually, a multi-layer solar cell has more than one junction inside the cell, these various layers can have extremely various I-V characteristics as shown in Fig. (2.21).
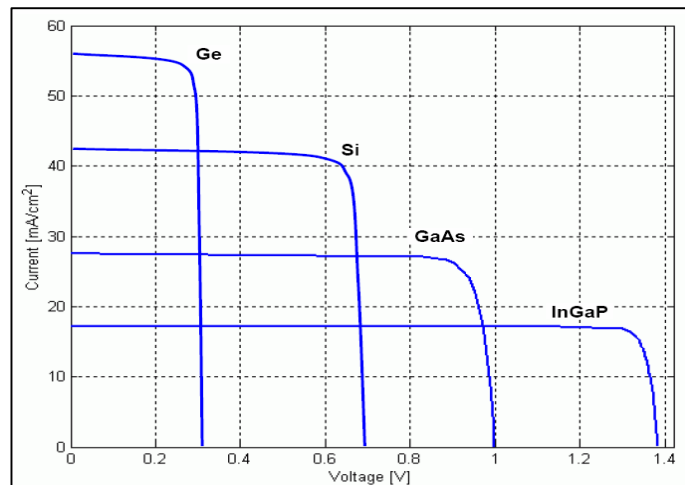


**Fig.(2.21)** (I-V) curves for solar cells depending on different Semiconductor Materials[64].

## 2.2.11 Multi-layer solar cell based on III- V

The basic limitation that multi-layer solar cells suffer from is the availability of materials with optimal bandgaps that permit at the same time high efficiency through out low defect densities. Alloys in the III-V groups especially both InGaP and GaAs, are considered the most promising material for solving these challenges and the manufacture of these cells. Those materials are also used in other different optical applications, like laser diodes, hetero-structures III-V, and high brightness LED[65].

The solar cells manufactured from III-V semiconductor compounds have the potential for high performance, their compound materials have advantages including the band gap tunability by elemental compositions covering a broad range of the solar spectrum, higher photon absorption by the direct band gap energies, higher resistivity against high-energy radiations in space, and smaller efficiency degradation by heat than Si solar cells. To produce high efficient power production from a tandem cell, every sub-cell current value must be matched at maximum power.

# CHAPTER 3

# THE SILVACO ATLAS SIMULATOR

In this thesis, a tandem solar cell is designed using an (InGaP/GaAs) structure. Silvaco software is used as a stimulating program. Various parameters of the cell were studied to find the effect of these parameters on the tandem cell efficiency, like temperature, cell thickness, and doping concentration.

## 3.1 <u>Introduction</u>

ATLAS has the ability to simulate a semiconductor accurately devices which is a very critical issue to industrials and research environments. The ATLAS simulation program is specifically developed for 2D and 3D modeling depending on the semiconductor components physics to comprise the electrical, thermal, and optical characteristics. ATLAS has a library of materials that is predefined for designing any semiconductor device after defining the size and dimension. This software offers several device examples to aid in new unique designs.

## 3.2 <u>The common inputs and outputs of ATLAS</u>

Two types of the input file are used for ATLAS:

- A text file containing orders from ATLAS.
- A structure file defining the structure to be simulated.

ATLAS generates three output file types:

- The runtime output, which presents the error messages and warning messages during the simulation process.
- Log file, which stores the currents and the voltages.
- The structure file, which saves 2D and 3D data file pertinent to solution variable values.

Fig (3.1) displays the inputs and outputs of Silvaco ATLAS.
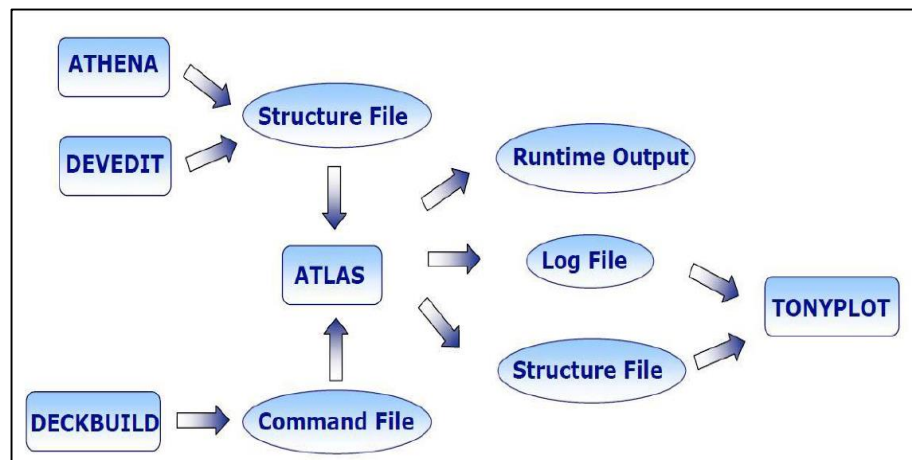


**Fig.(3.1)** Inputs and outputs of Atlas[66].

## 3.3 **DeckBuild**

Deckbuild is the run-time environment utilized to input a command file or deck, and is denoted by the extended ".in". To execute ATLAS inside the Deck Build environment, the first step is to use the command line:

**go atlas**

After this command, the input data file should follow the sequence of commands illustrated in Fig (3.1).

Table (3.1) shows the primary groups of statements. Failure to respond to this order may not only result in program termination, but also untrue functioning and wrong outcomes.

**Table (3.1)** The order of Atlas command[67].

| Group | | Statements |
|---|---|---|
| 1. Structure Specification | ── | MESH REGION ELECTRODE DOPING |
| 2. Material Models Specification | ── | MATERIAL MODELS CONTACT INTERFACE |
| 3. Numerical Method Selection | ── | METHOD |
| 4. Solution Specification | ── | LOG SOLVE LOAD SAVE |
| 5. Results Analysis | ── | EXTRACT TONYPLOT |

## 3.4 Structure Specification

The specification for the structure is made by defining the mesh, region, electrodes, and levels of doping.

### 3.4.1 Mesh

The first step for the construction of a device is to specify the mesh. The mesh is a grid covering the physical region in which the equipment is built and simulated. The mesh is formed by a number of horizontal and vertical lines with a user-set distance from each other[68]. In this thesis, the mesh utilized is a two-dimensional (2D). The public format for defining the mesh is:

x.mesh location=<value> spacing=<value>
y.mesh location=<value> spacing=<value>

The default space value is one, however, you may replace the value of less than one to create a finer mesh or a coarse mesh by replacing a value higher than one [69]. The advantage of a coarse mesh is a quicker simulation speed but on the other hand, it gives a lesser accurate model, the reverse is true for a fine mesh. The two lines include the statements.(x.mesh and y.mesh) Figure (3.2) offers an example of a finer mesh and coarser mesh in ATLAS.
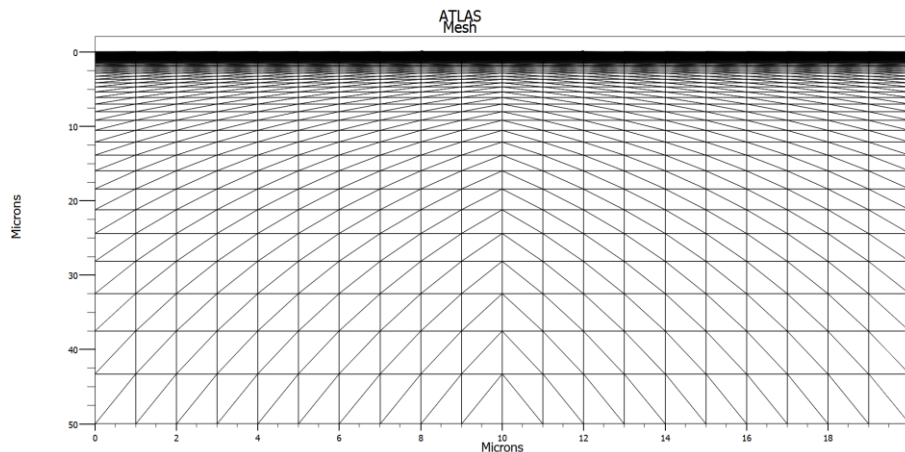


**Fig.(3.2)** Mesh in ATLAS.

The solar cell's electrical properties are assessed at each cross of horizontal and vertical lines specified in the mesh to determine the performance of the solar cell and the resolution of the simulation [70]. To simulate multilayer solar cell tunnel junctions, a special kind of mesh is used and it is known as Quantum tunnel mesh. Similar to normal meshing, in quantum tunnel mesh instructions, the programmer employs the following basic format:

qtx.mesh location=<value> spacing=<value>
qty.mesh location=<value> spacing=<value>

In the tandem cell, the current flows through the tunnel diode and lies above the previously formed mesh. Because of the current flow in the y-direction via the tunnel diode, spacing is considerably finer in this direction, but the spacing in the X-direction is bigger. The following statements are examples of special quantum tunnel mesh.

qtx.mesh loc=0.0     spac=0.25

qtx.mesh loc=1.0     spac=0.25

qtx.mesh loc=0.67    spac=0.0002

qty.mesh loc=0.685   spac=0.0001

qty.mesh loc=0.7     spac=0.0002

### 3.4.2 Region

The second step in building a semiconductor device is dividing the generated mesh into multiple regions. For each region, the code assigns the material. Color-coding is used to identify the material .The general format used to define the region is:

region number=<integer> <material type> \ <position parameters>

  For an example:

region num=4 material=InGaP  x.comp=0.49 x.min= - 250 \ x.max=25 y.min=-0.85 y.max=-0.65 .

The symbol (\) in this example implies that the command is continued in the next line. The x and y composite fractions (x.comp and y.comp) must be mentioned in region instructions for materials of a particular mole fraction. Parameters of position are identified by x.min, x.max, y.min, and y.max.

Fig. (3.3) provides an example of the regions created in a semiconductor device.
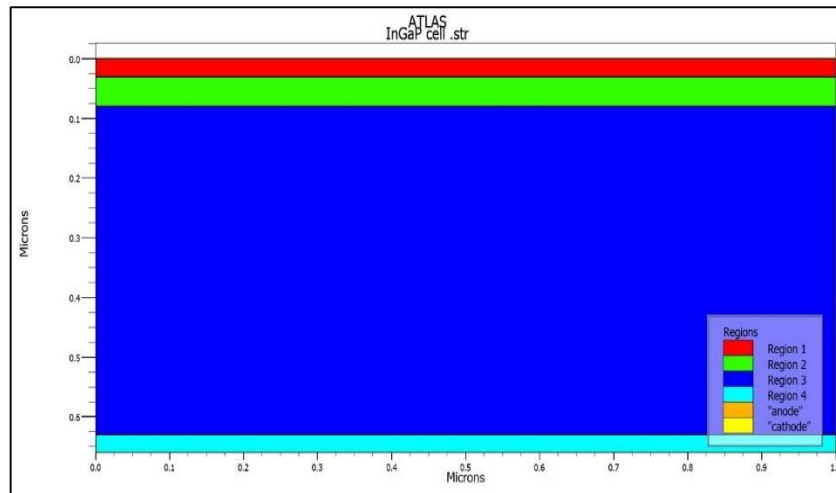
**Fig.(3.3)** The regions for an InGaP solar cell in ATLAS.

### 3.4.3 Electrodes

Although the Silvaco program can specify up to 50 electrodes for single-layer solar cells, only the anode and cathode are required[70]. The anode is the first electrode that was specified on the top of the tandem in multi-junction solar cells. The anode is aluminum and it just covers around 8% or less of the top.  The cathode is the second electrode that was specified at the bottom of the tandem and it covers the whole bottom surface of the solar cell. Fig (3.4) illustrates location of the electrodes. The general statements used to define electrodes are:

electrode name=anode                                  top

electrode name=cathode                              bottom
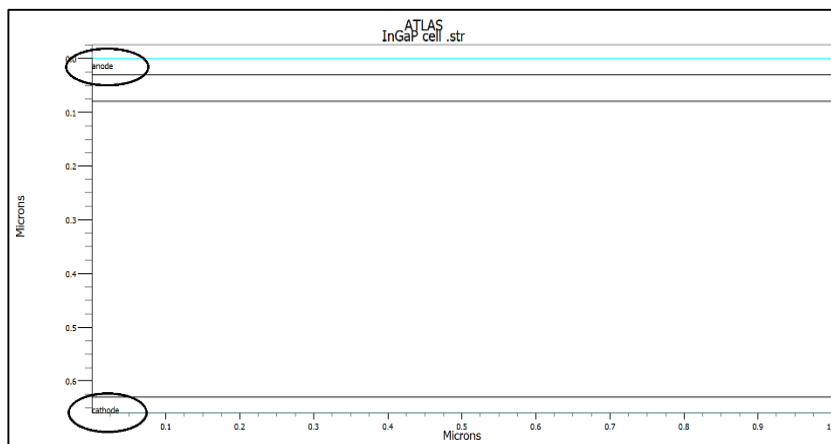


**Fig.(3.4)** InGaP cell electrodes.

36

### 3.4.4 Doping

The final part of structure specification is doping, which is defined for all regions of the semiconductor device. The general format of the doping statements is as the following:

doping <distribution_type> <dopant_type> \ <position_parameters>

In each part of the solar cell, the doping statements define the kind and amount of doping. The next doping statements show how this is accomplished.

doping uniform region=5 n.type conc=5e18
doping uniform region=6 p.type conc=1e16

The doping can be either n-type or p-type and the distribution function type is either uniform or Gaussian[71]. The doping profile is shown in Fig (3.5).
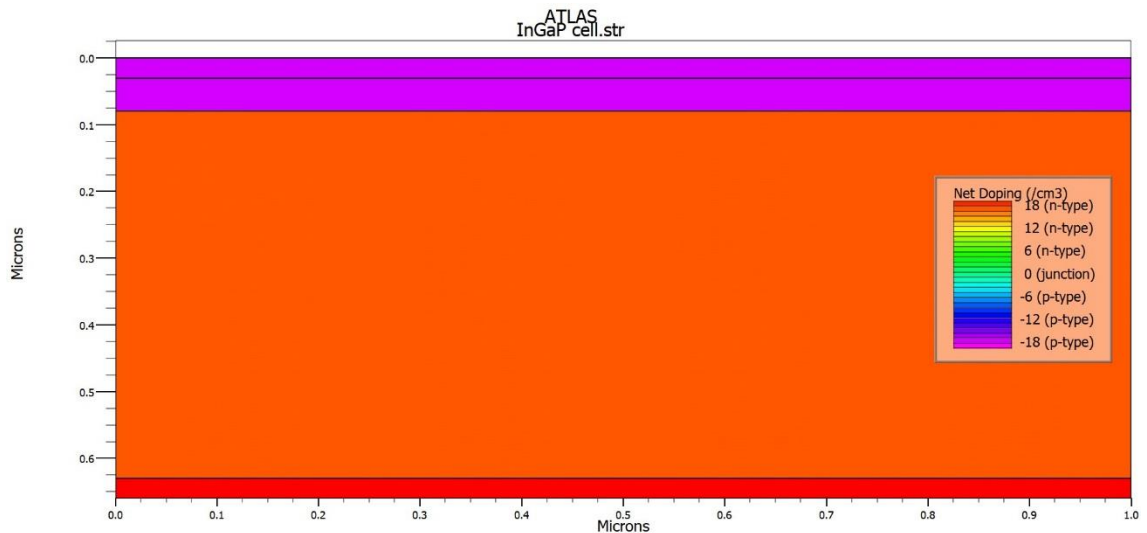


**Fig.(3.5)** The doping profile for InGaP cell.

## 3.5 Material Model Specifications

Material specification is split into material, models, contact, and interface as illustrated in Fig. (3.6).



**Fig.(3.6)** Material model specification in ATLAS [54]

## 3.5.1 Material

When the structure of the device has been fully assembled, the materials utilized to create the device must be described by themselves. The material statement permits the identification of several fundamental parameters. These values could be applied to material or region [68].

material <localization> <material_definition>

The following examples show various methods in which materials can be specified:

material material=silicon eg300=1.1 mun=1200
material name=emitter nc300=1.3e20 nv300=1.28e19

Where (eg300) is the room temperature bandgap, (mun) is electron mobility, (nv300) is valence band density of states at room temperature, and (nc300) is conduction band density of states at room temperature. Other semiconductor parameters should be defined or else ATLAS will use a default value.

### 3.5.2 Models

The models are divided into five sections: mobility, recombination, carrier statistics, impact ionization, tunneling. The following is the syntax of the model statement:

models <model flag><general parameter> /<model dependent parameters>

The selection of the model relies on the materials chosen for simulation.

The following example activates sundry models.

models  bgn conmob srh

- **CONMOB**: standard concentration dependent mobility model.
- **SRH**: Shockley-Read-Hall recombination.
- **BGN**: band-gap narrowing.

### 3.5.3 Contact

Contact sets the features of the electrode. The expression of contact is as follows:

contact number=<n> |name=<name>|all

here is an example of the statement of contact:

contact name=anode work function=4.1

This statement is not needed if the characteristics of electrodes do not require specialized designation or adjustment[70].

### 3.5.4 Interface

The interface statement defines the insulator or semiconductor boundaries. In the following is the syntax:

interface [<parameters>]

The use of the interface statement can be shown in the following example:

interface x.min=-5 x.max=5 y.min=-0.1 y.max=5 \ QF=1e12 s.n=1e6
s.p=1e6

The boundaries are determined by the max and min values. The QF value defines the density of the fixed oxide charge (cm$^{-2}$). Nevertheless, in this thesis interface characteristics are not defined in the simulated tandem cell.

## 3.6 Numerical Method Selection

The selection of the numerical method should be defined after the materials model specification step, see Fig (3.7). For calculating solutions of semiconductor issues, many different numerical methods exist.



**Fig.(3.7)** Selection of the numerical method in Atlas [54].

In the Silvaco Atlas there are many kinds of solutions:

GUMMEL, NEWTON, BLOCK

The GUMMEL method solves every unknown and retaining constant variables, and repeats the operation until achieving a stable solution. The Newton method solves all unknowns concurrently. The Block method solves some of the equations by the Gummel method and solves others by using the Newton method.

The example below demonstrates the method statement usage:

method Gummel Newton

### 3.7 Solution Specification

Solution specification is classified into: log, solve, load, and save statements, as demonstrates in Fig. (3.8).
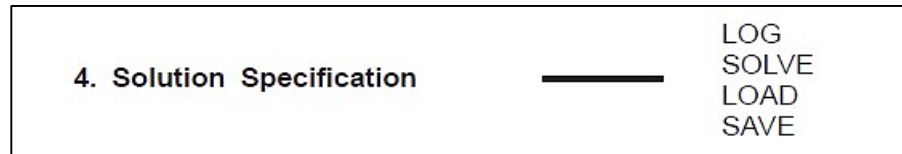


**Fig.(3.8)** Solution specification in Atlas[54].

### 3.7.1 Log

LOG files save the terminal characteristics calculated by ATLAS. DC or AC data are created via a SOLVE statement after a LOG statement is saved. The LOG file is specified as the following:

log outf=Tandem.log

The example stores the results information into Tandem.log.

### 3.7.2 Solve

The solve statement guides ATLAS to do a solution to one or more determined bias points. An example of solve statement that was used in this study is:

solve b1=1

(b1) determines the optical power equivalent to (1sun) (beam numbers 1). For this thesis, the spectrum of AM1.5 is utilized in a terrestrial application to collect the energy from the solar cell.
An optical beam is modeled by employing the beam statement as follow:

beam <parameters>.

The beam origin is determined through x.origin and y.origin parameters, the angle parameter is defined by the beam propagation direction relative to the x-axis, whereas the angle=90.

Beam is the beam number of the optical beam during analyzing AC photogeneration. After applying the light source (beam statement), the solution may be attained at various electrode voltages to establish the I-V solar cell curve:

solve vanode=0.0   name=anode. vstep=0.1 vfinal=2.7

I-V curve is derived by sweeping over anode voltages of 0.0 V to $V_{OC}$ for the solar cell. The outcomes can be shown through the Tony Plot of Silvaco.

### 3.7.3 LOAD and SAVE

The **load** statement includes prior solutions of files as first guess to the other bias points. All anode points information is entered into an output file via the save statement.  Example of load and save statements are shown below:

save outf=Tandem.str

load infile=Tandem.str

### 3.8 Results Analysis

The data can be extracted and displayed graphically by Tony Plot. Also device parameters could be extracted, as demonstrated in Fig (3.9) using the **extract** statement:
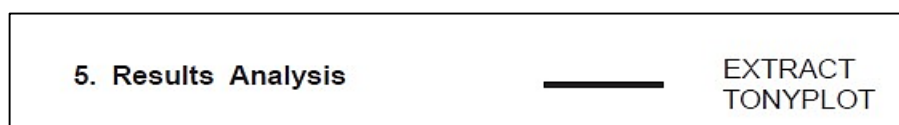


**Fig.(3.9)** Results analysis in Atlas[54].

The extract statement in the following example gives the current and the voltage characteristics for the solar cell. These data are stored in the data file ivcurve.dat.

Next, Tony Plot sketches the data graphically in the JVcurve.dat file, then Tony Plot records the information.

extract name="jv" curve (v."anode", j."cathode") /

outfile="jvcurve.dat"

tonyplot jvcurve.dat

The (J-V) characteristics curve sketched using Tony Plot is displayed in Fig. (3.10).
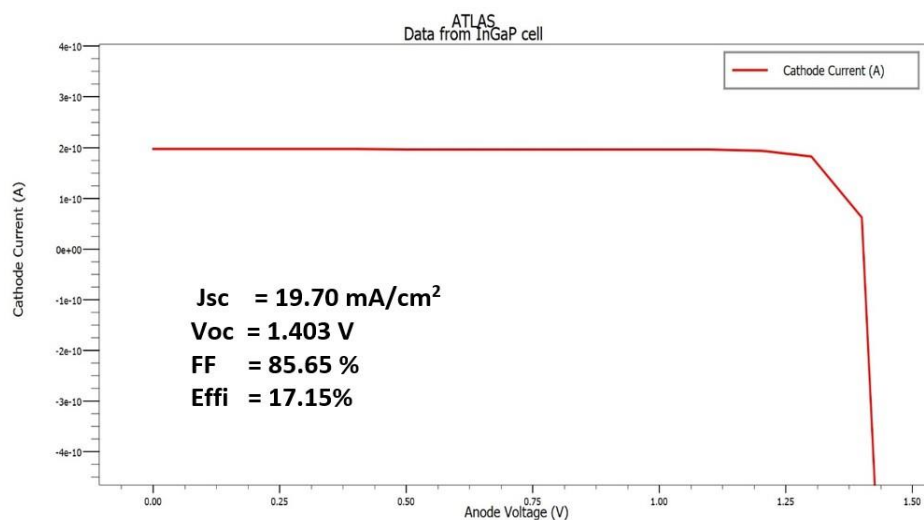


**Fig.(3.10)** The J-V curve of the (InGaP) cell.

A profile was immediately executed after the design was constructed and run, allowing the designer to forecast which values of the tandem cell parameters provided the optimum output power into the ATLAS design of the tandem cell as seen in chapter 4.

# CHAPTER 4

## SIMULATION AND RESULTS OF TANDEM CELL

## 4.1 Introduction

In this chapter, the tandem cell was divided into an InGaP sub cell and a GaAs sub cell, and each sub cell was numerically simulated as a first step. The next step is to conduct a complete tandem implementation after a final design has been obtained from the experimental top and bottom sub cells that joined to each other by a tunnel junction. In the final step, we will display the results of the designed structures that were simulated.

## 4.2 The Materials that Used in tandem Cell simulation

### 4.2.1 Indium Gallium Phosphide (InGaP)

InGaP is a semiconductor material that has a wide bandgap (1.86 – 1.9 ) eV [72][73] and is lattice-matched to GaAs and Ge materials. The direct bandgap and high  absorption rate are important properties of InGaP[74]. An InGaP cell is the better option for the upper part in tandem cell structure due to its wider bandgap and matched lattice to GaAs and Ge[75].  The parameters group of the ternary material InGaP is illustrated in Table (4.1).

**Table (4.1)**   GaInP parameters[76][77].

| Parameters | InGaP |
|---|---|
| $E_g$ (eV) | 1.9 |
| Electron affinity   (eV) | 4.16 |
| Lattice Constant    (Å) | 5.65 |
| Permittivity  $\varepsilon$ | 11.6 |
| $N_c$  (cm$^{-3}$) | 1.30E + 20 |
| $N_v$  (cm$^{-3}$) | 1.28E + 19 |
| $\mu_n$ electron mobility ( cm$^2$ . v$^{-1}$ s$^{-1}$) | 1945 |
| $\mu_h$ hole   mobility  ( cm$^2$ . v $^{-1}$ s$^{-1}$) | 141 |

### 4.2.2 Indium Aluminum Gallium Phosphide (InAlGaP)

InAlGaP is a semiconductor material with a nearly identical lattice constant to GaAs, it has a large bandgap that absorbs shorter wavelength solar irradiations. The InAlGaP bandgap is equal to 2.3 eV.

InAlGaP layers are used, as a window layer and back surface field (BSF) layer. Typically, the window layer is composed of wide band gap materials, allowing a maximum solar irradiance to reach the device [89]. The parameters of InAlGaP are listed in Table (4.2).

**Table (4.2)**    InAlGaP parameters[76] [77]

| Parameters | InAlGaP |
|---|---|
| $E_g$ (eV) | 2.3 |
| Electron affinity (eV) | 4.2 |
| Lattice Constant (Å) | 5.65 |
| Permittivity ε | 11.7 |
| $N_c$ (cm$^{-3}$) | 1.20E + 20 |
| $N_v$ (cm$^{-3}$) | 1.28E + 19 |
| $\mu_n$ electron mobility ( cm$^2$ . v$^{-1}$ s$^{-1}$) | 2150 |
| $\mu_h$ hole mobility   ( cm$^2$ . v $^{-1}$ s$^{-1}$) | 141 |

### 4.2.3 GaAs (Gallium Arsenide)

GaAs semiconductor material has a direct and wide bandgap[78]. This material is commonly used for space applications due to its very high luminous absorption coefficient, high performance ,reliability, and higher temperature resistance[79]. The high electron mobility of GaAs (8800) cm$^2$/Vs provides higher performance compared to silicon. Table (4.3) shows the parameters of GaAs material.

**Table (4.3)** GaAs parameter set[80][81]

| Parameters | GaAs |
|---|---|
| $E_g$ (eV) | 1.42 |
| Electron affinity (eV) | 4.07 |
| Lattice Constant (Å) | 5.65 |
| Permittivity $\varepsilon$ | 13.1 |
| $N_c$ (cm$^{-3}$) | 4.7E+17 |
| $N_v$ (cm$^{-3}$) | 7.0E+18 |
| $\mu_n$ electron mobility ( cm$^2$ . v$^{-1}$ s$^{-1}$) | 8800 |
| $\mu_h$ hole mobility   ( cm$^2$ . v $^{-1}$ s$^{-1}$) | 400 |

The simulations were performed using the standard spectrum (1 sun) AM1.5 in the Silvaco Atlas device simulator and at 300 K operating temperature. The standard spectrum (Air Mass1.5 1000 W/m$^2$) was used to illuminate the cells in the simulators as shown in Fig. (4.1).
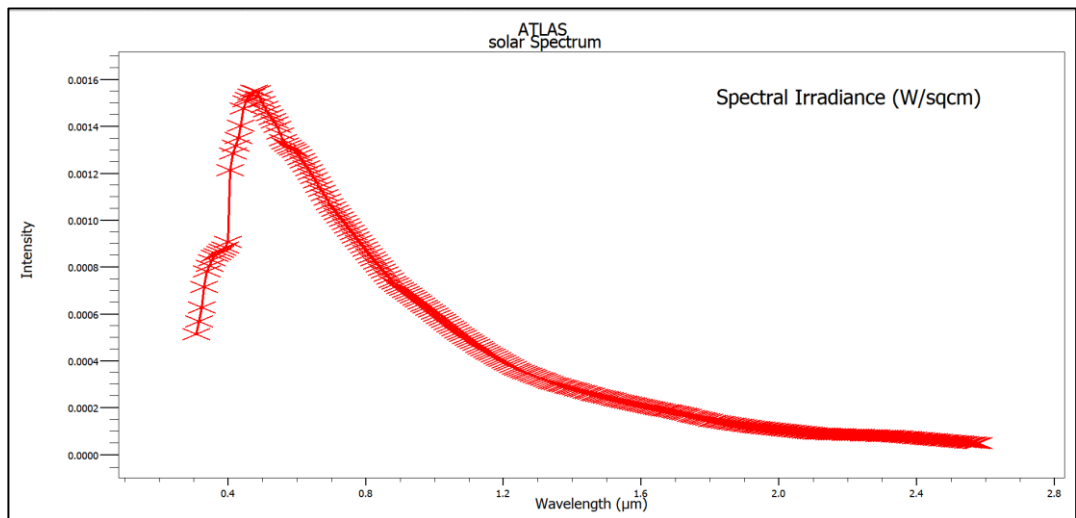


**Fig.(4.1)** Spectrum AM1.5 used to illuminate the model

## 4.3 (InGaP) Cell Simulation (upper cell)

InGaP cell is designed and simulated as a top cell. This cell consists of a base of n-InGaP of (0.55μm), a p-InGaP emitter of (0.05μm), (0.03μm) of a p-InAlGaP as a window layer, and (0.03μm) of an n-InAlGaP as BSF. Fig. (4.2) describes the graphical diagram of fallen light on the InGaP solar cell [88].
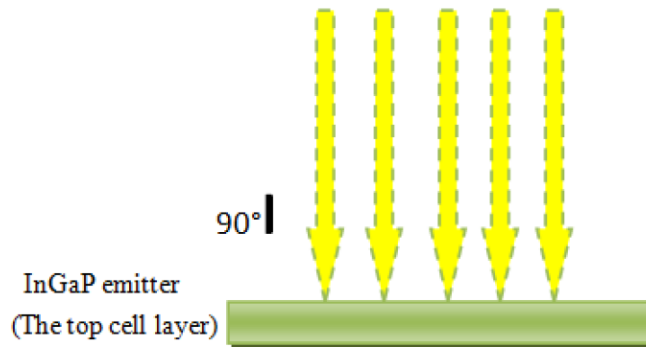


**Fig.(4.2)** Graphical diagram of incident light on the top solar cell layer. [82]

The diagram structure in Fig. (4.3) contains all information, such as layer thickness and doping concentration.



**Fig.(4.3)** Schematic diagram of the proposed (InGaP) cell.

The various compound materials utilized in the cell design are compatible with each other. From the following equations (4.1–3), the lattice constant of quaternary material (InAlGaP) are determined[77]:

$$a ( In_xAl_{1-x}P) = x \times (InP) + (1-x) \times a (AlP) \tag{4.1}$$

$$a (In_xGa_{1-x}P) = x \times (InP) + (1-x) \times a (GaP) \tag{4.2}$$

$$a (In_x(Al_yGa_{1-y})_{1-x}P) = y \times (InAlP) + (1-y) \times a (InGaP) \tag{4.3}$$

## 4.4 (GaAs) CELL SIMULATION (lower cell)

The GaAs solar cell is the next cell to model. This cell consists of n-GaAs base of (2µm), p-GaAs emitter of (0.5µm), p-InGaP window of (0.04µm), (0.1µm) of n-InAlGaP as (BSF) layer, and n-GaAs substrate of (0.2µm).The diagram structure in Fig. (4.4) contains all information such as layer thickness and doping concentration of the GaAs cell.

| | Anode Contact | | |
|---|---|---|---|
| 0.04 µm | window | $In_{0.49}Ga_{0.51}P$ | $P = 3e18\ cm^{-3}$ |
| 0.50 µm | Emitter | GaAs | $P = 2e18\ cm^{-3}$ |
| 2.00 µm | Base | GaAs | $n = 2e17\ cm^{-3}$ |
| 0.10 µm | BSF | $In_{0.5}(Al_{0.7}Ga_{0.3})_{0.5}P$ | $n = 5e18\ cm^{-3}$ |
| 0.20 µm | Substrate | GaAs | $n = 1e18\ cm^{-3}$ |
| | Cathode Contact | | |

**Fig.(4.4)** Schematic diagram of the proposed (GaAs) cell.

## 4.5 The tandem cell modelling

The tandem cell (InGaP/GaAs) is designed and built as shown in the diagram structure of Fig. (4.5). This figure contains all information such as layer thickness and doping concentration. Thicknesses and base parameters for layers of the two cells InGaP and GaAs were kept the same as in the individual design. The GaAs tunnel diode is utilized to link the top and bottom cells. The top cell's energy gap (Eg) is 1.86 to 1.9 eV that absorbs the majority of the short wavelength and transfers long wavelengths to the lower cell. The base cell's Eg is 1.42 to 1.43 eV. In this design, InGaP is used as a thin top cell to achieve current matching between the top and bottom cell and also for achieving the high efficiency of this tandem cell[83].

| | | **Anode Contact** | | |
|---|---|---|---|---|
| 0.03 μm | window | $In_{0.5}(Al_{0.7}Ga_{0.3})_{0.5}P$ | P = 2e18 cm$^{-3}$ | |
| 0.05 μm | Emitter | $In_{0.49}Ga_{0.51}P$ | P = 2e18 cm$^{-3}$ | |
| 0.55 μm | Base | $In_{0.49}Ga_{0.51}P$ | n = 7e16 cm$^{-3}$ | |
| 0.03 μm | BSF | $In_{0.5}(Al_{0.7}Ga_{0.3})_{0.5}P$ | n = 2e18 cm$^{-3}$ | |
| 0.025 μm | Tunnel Diode | GaAs | n = 5e19 cm$^{-3}$ | |
| 0.025 μm | Tunnel Diode | GaAs | P = 3e19 cm$^{-3}$ | |
| 0.04 μm | window | $In_{0.49}Ga_{0.51}P$ | P = 3e18 cm$^{-3}$ | |
| 0.50 μm | Emitter | GaAs | P = 2e18 cm$^{-3}$ | |
| 2.00 μm | Base | GaAs | n = 2e17 cm$^{-3}$ | |
| 0.10 μm | BSF | $In_{0.5}(Al_{0.7}Ga_{0.3})_{0.5}P$ | n = 5e18 cm$^{-3}$ | |
| 0.20 μm | Substrate | GaAs | n = 1e18 cm$^{-3}$ | |
| | | **Cathode Contact** | | |

**Fig.(4.5)** Full Schematic diagram of the proposed tandem cell.

## 4.6 RESULTS AND DISCUSSION

### 4.6.1 The upper cell (InGaP) results

To adjust the energy bandgap of the $In_{1-x}Ga_xP$ cell on the value 1.87 eV, the effect of varying the value of mole fraction (x) for Gallium concentration from 0 to 0.49 is studied. It is observed that the energy of a photon is absorbed in different ways because the energy gap would be modified by depending on the (Ga) content(x).The result of the simulation is presented in Table 4.4.

**Table (4.4)** $(Ga_x)$ mole fraction changing simulation

| Mole fraction (x) | Bandgap(Eg) (eV) | $J_{SC}$ (mA/ cm$^2$) | $V_{OC}$ (V) | FF (%) | Efficiency (ŋ) (%) |
|---|---|---|---|---|---|
| 0 | 1.35 | 7.33 | 1.11 | 71.50 | 4.24 |
| 0.1 | 1.43 | 7.36 | 1.11 | 71.33 | 4.25 |
| 0.2 | 1.52 | 7.43 | 1.22 | 72.92 | 4.81 |
| 0.3 | 1.63 | 20.39 | 1.16 | 82.40 | 14.19 |
| 0.4 | 1.75 | 20.03 | 1.28 | 83.90 | 15.66 |
| 0.49 | 1.87 | 19.70 | 1.40 | 85.65 | 17.15 |

With increasing the composition of (Ga), the energy gap widens, allowing it to collect further photons at the region. That means enhancing the current density and increasing the efficiency. The InGaP cell is designed and simulated successfullys as mentioned in Fig. (4.2), and Fig. (4.6) show the (InGaP) simulated cell in ATLAS programme.
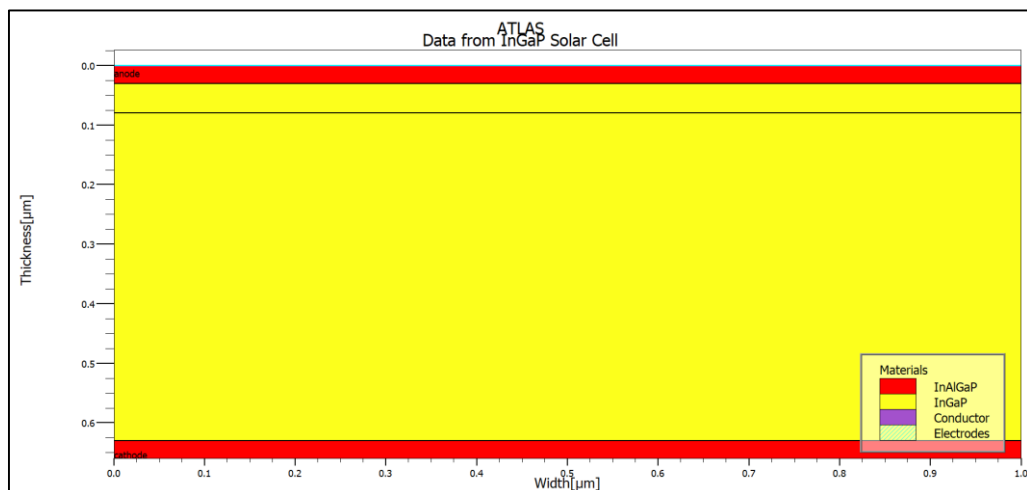


**Fig.(4.6)** InGaP solar cell structure ATLAS simulated.

Wider bandgap material is needed to collect further electrons to the other terminal. Fig. (4.7 (a)) shows that InAlGaP's high band gap provides higher barrier for minority carriers, that lead to reduce the recombination near the surface terminal .Fig. (4.7(b)) shows the potential development plus band alignment within the cell's range which depends on the material's bandgap and physical characteristics. Fig. (4.8) shows the current density-voltage (J-V) curve of the modeled structure.
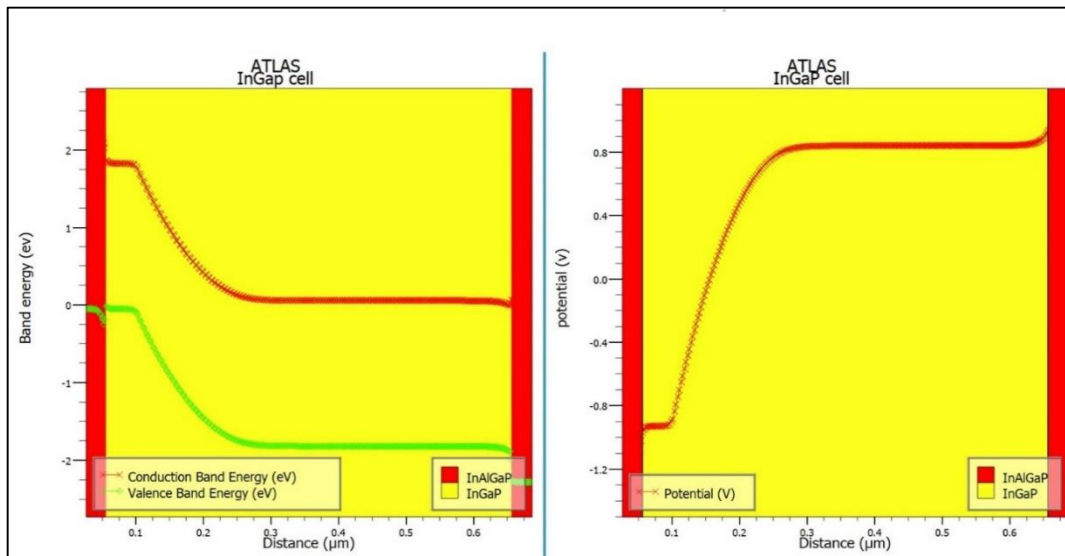


**Fig.(4.7)** (a)Energy band structure        (b) Potential growth in the InGaP.
in the InGaP.
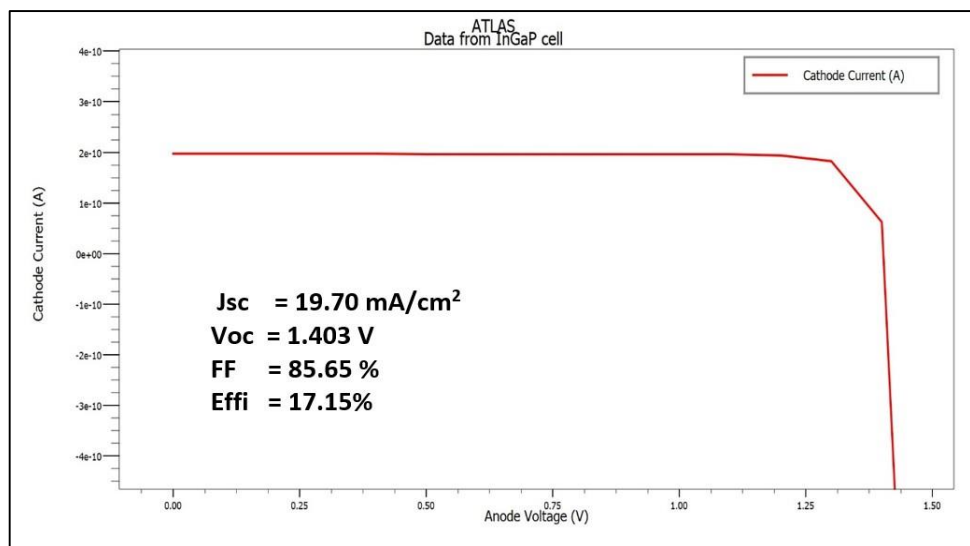


**Fig.(4.8)** J–V Characteristics of InGaP solar cell

The external quantum efficiency (EQE) and the mesh of the InGaP cell is shown in Fig. (4.9), Fig. (4.10)  respectively
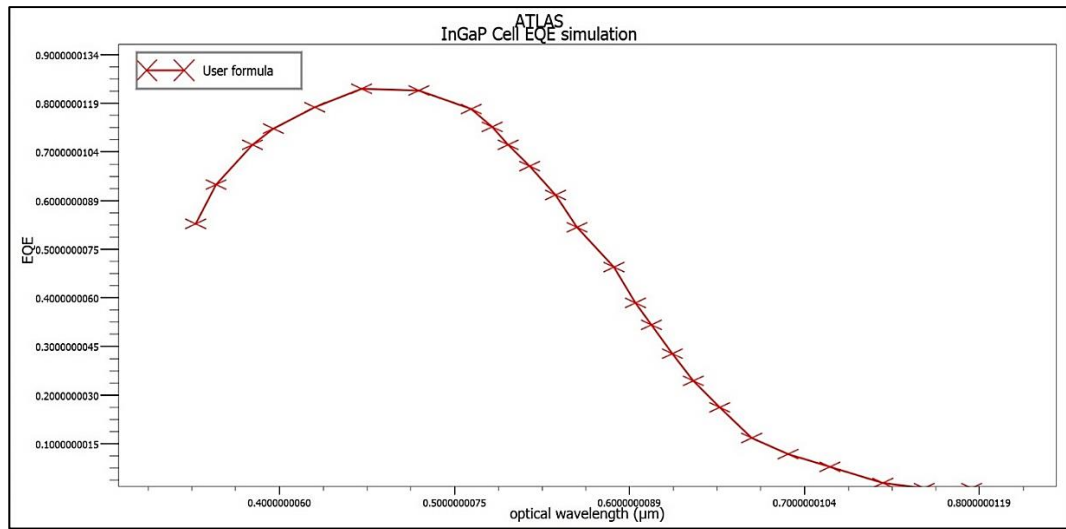


**Fig.(4.9)** EQE of the InGaP cell
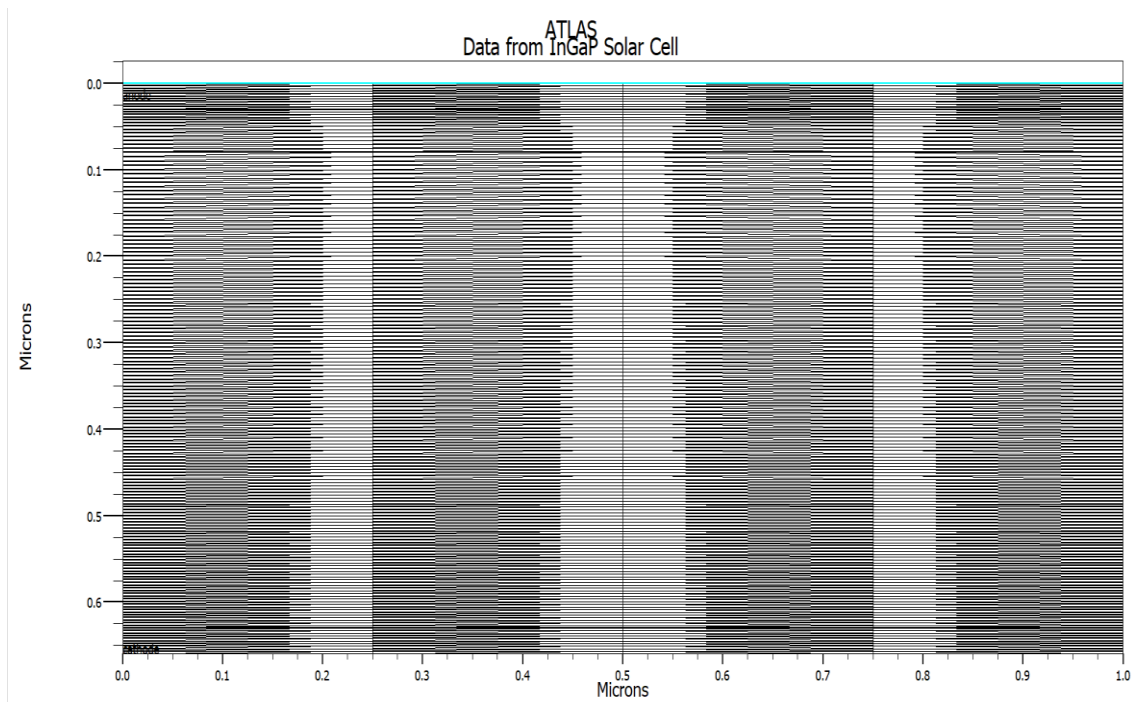


**Fig.(4.10)** Generated mesh of (InGaP) cell

Equation (2.21) is applied depending on the band gap of InGaP cell that equal to 1.87 eV to determine the wavelength as shown:

$$\lambda(\mu m) \ \leq \ \frac{1.24}{Eg(ev)}$$

$$\lambda(\mu m) \leq \frac{1.24}{1.87} \leq 0.663 \ \mu m.$$

InGaP solar cell absorbs the ultraviolet part and visible part of the spectrum, which is exactly clear in Fig (4.9) where the cell absorbs the short-wavelength light from 0.3 µm to 0.675 µm.

## 4.6.2 The lower cell (GaAs) results

Lower cell (GaAs) is the next cell that is designed and simulated as mentioned in Fig. (4.3). The first step in the modeling is to determine the mesh to be used for the cell as seen in Fig. (4.11). Fig. (4.12). shows the (GaAs) simulated cell in ATLAS, programme.
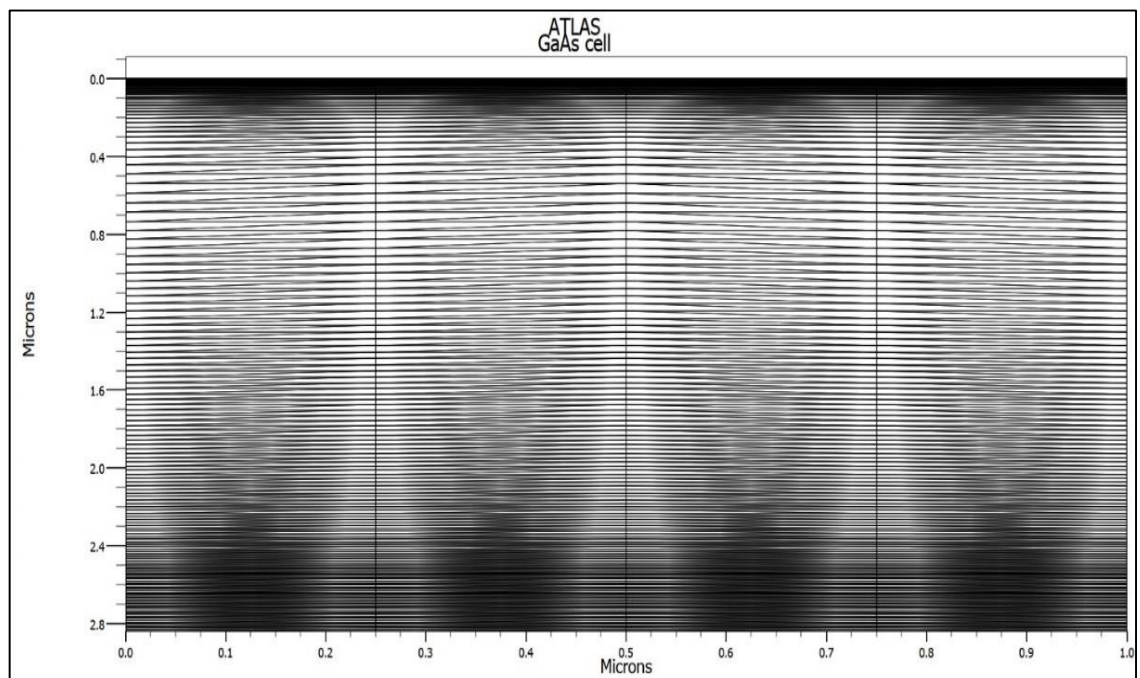


**Fig.(4.11)** Generated mesh of (GaAs) cell.
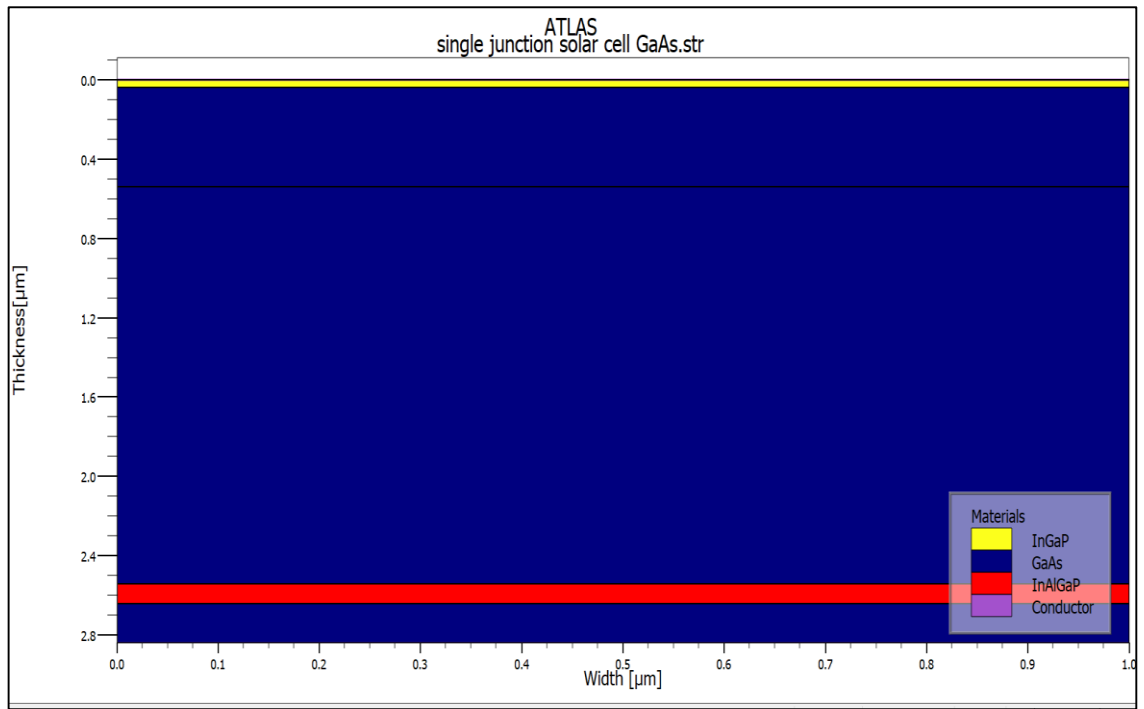
**Fig.(4.12)** The structure of GaAs cell simulated in ATLAS.

Additionally, Fig. (4.13) shows the current density-voltage curves (J-V) of the simulated cell structure characteristics. It is clear that the cell shows an identical characteristics.



Jsc  = 35.74 mA/cm²
Voc = 1.0050 V
FF    = 88.64 %
Effi  = 23.071%
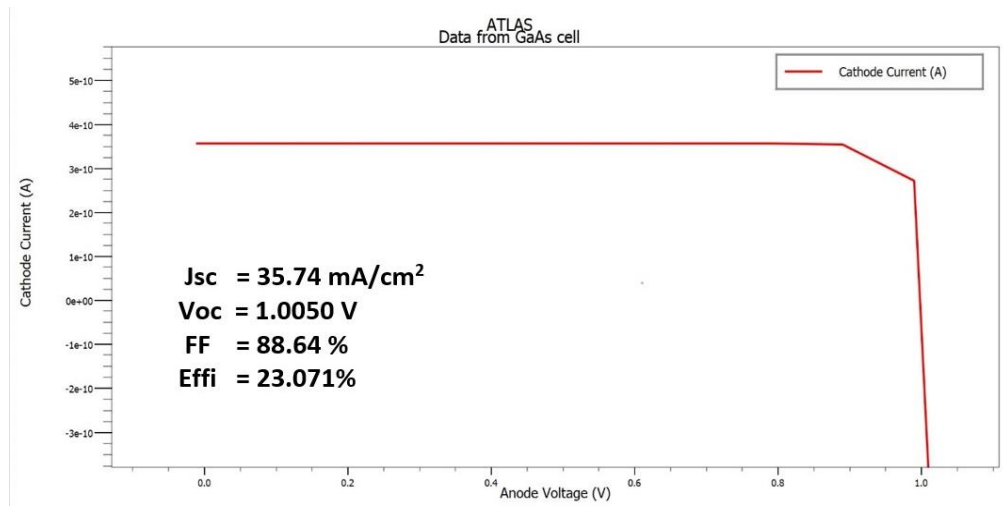
**Fig.(4.13)** J–V Characteristics of GaAs solar cell

In the next Fig. (4.14 (a)), the energy band structure of the GaAs cell is illustrated, the potential growth inside the cell under standard (1 sun) AM1.5 illumination is illustrated in Fig. (4.14 (b)).
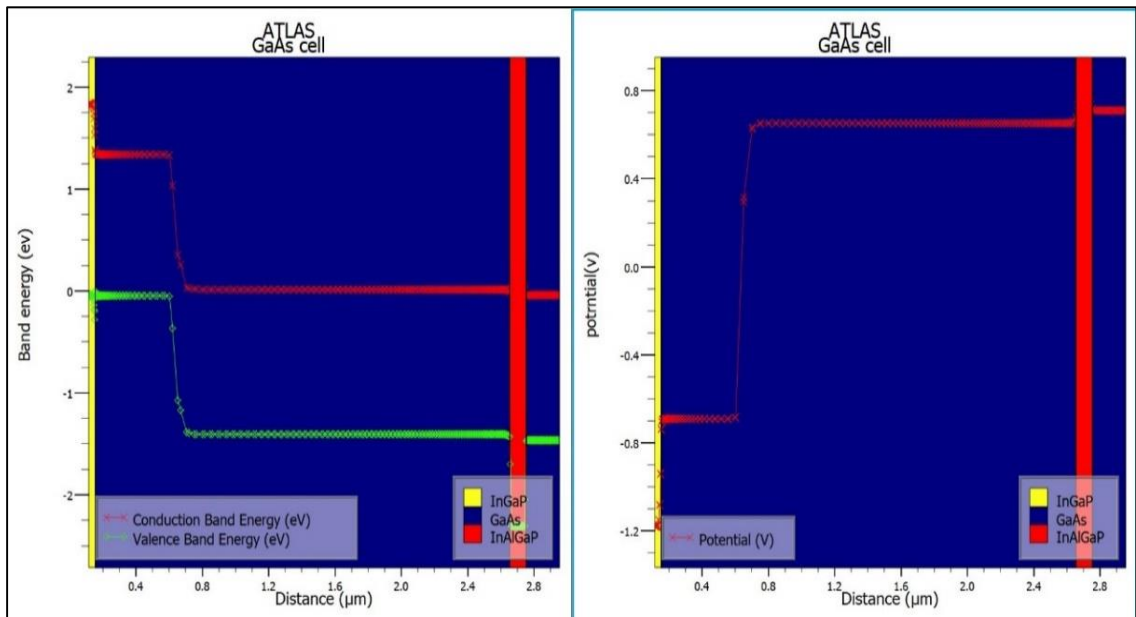
**Fig.(4.14)** (a) Energy band structure in the GaAs.      (b) Potential growth in the GaAs.

Finally, Fig. (4.15) shows the external quantum efficiency (EQE) of the GaAs cell.
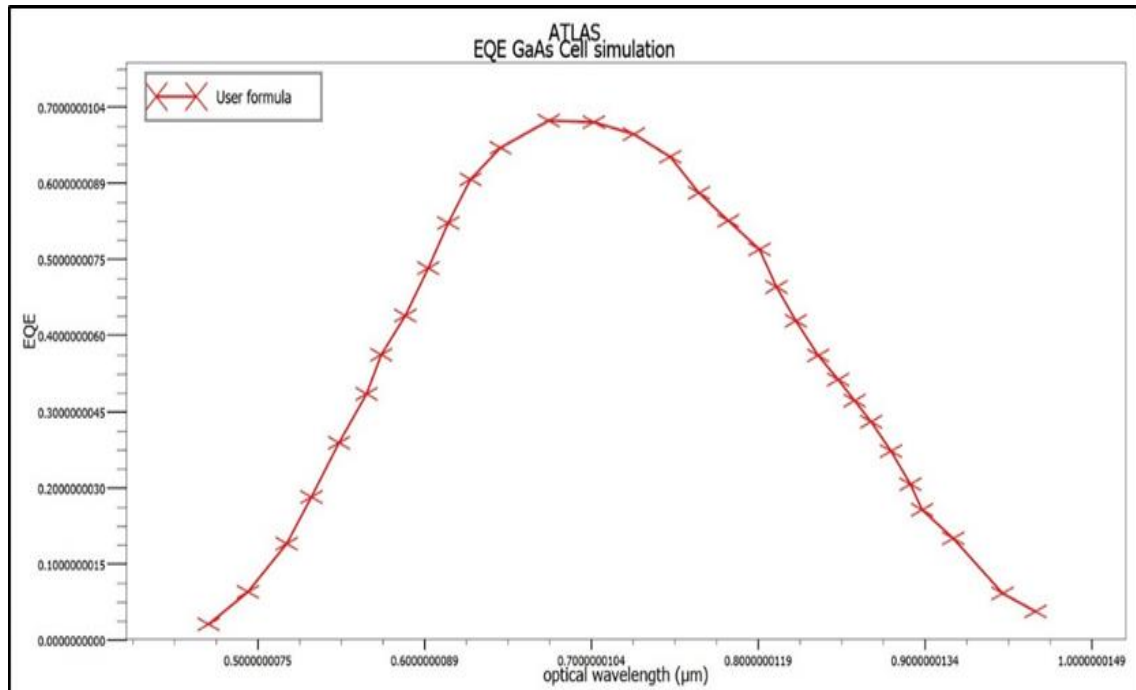


**Fig.(4.15)** EQE of the GaAs cell.

The wavelength eq. (2.21) has been applied depending on the bandgap of GaAs cell that equal to1.42 eV to determine the wavelength as seen:

$$\lambda(\mu m) \leq \frac{1.24}{Eg(ev)}$$

$$\lambda(\mu m) \leq \frac{1.24}{1.42} \leq 0.873 \ \mu m$$

GaAs solar cell absorbs the longer wavelength (i.e. near infrared part of the spectrum of light), this is exactly clear in Fig. (4.15) where the GaAs cell starts absorbing the wavelengths from 0.5 to 0.9 μm.

### 4.6.3 The tandem cell (InGaP/GaAs) results

After building a full tandem cell by linking the top cell with the bottom cell throughout tunnel junction (GaAs), the first step in the tandem cell modelling is to determine the mesh to be used for the equipment as shown in Fig. (4.16). Then the tandem simulated cell is described in Fig. (4.17). Finally, Fig. (4.18) present the proposed tandem cell model doping profile.
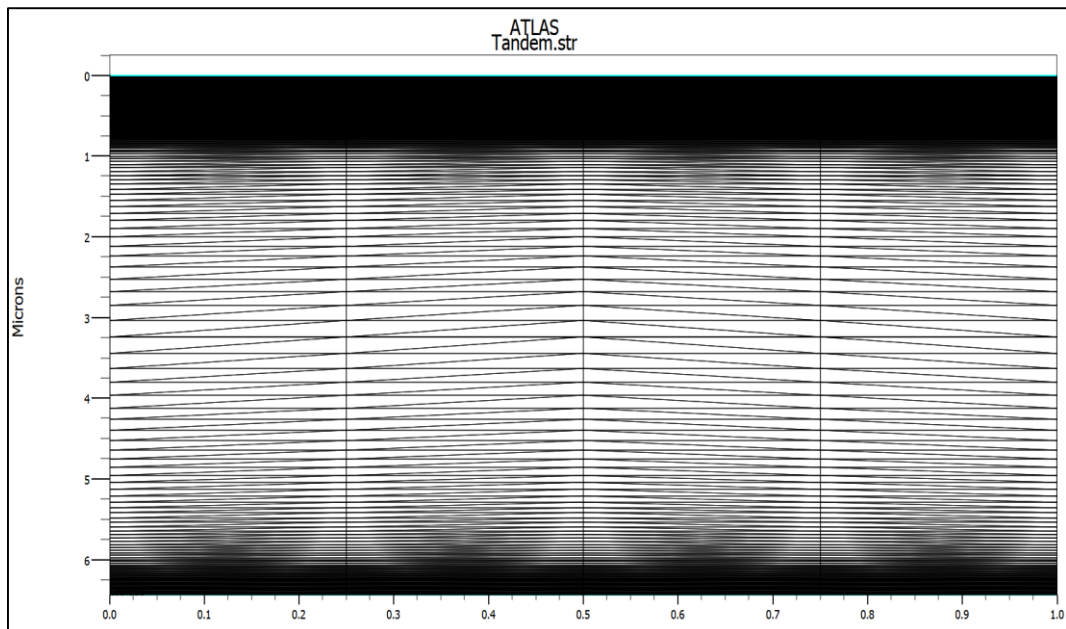


**Fig.(4.16)** Mesh profile of the designed structure.
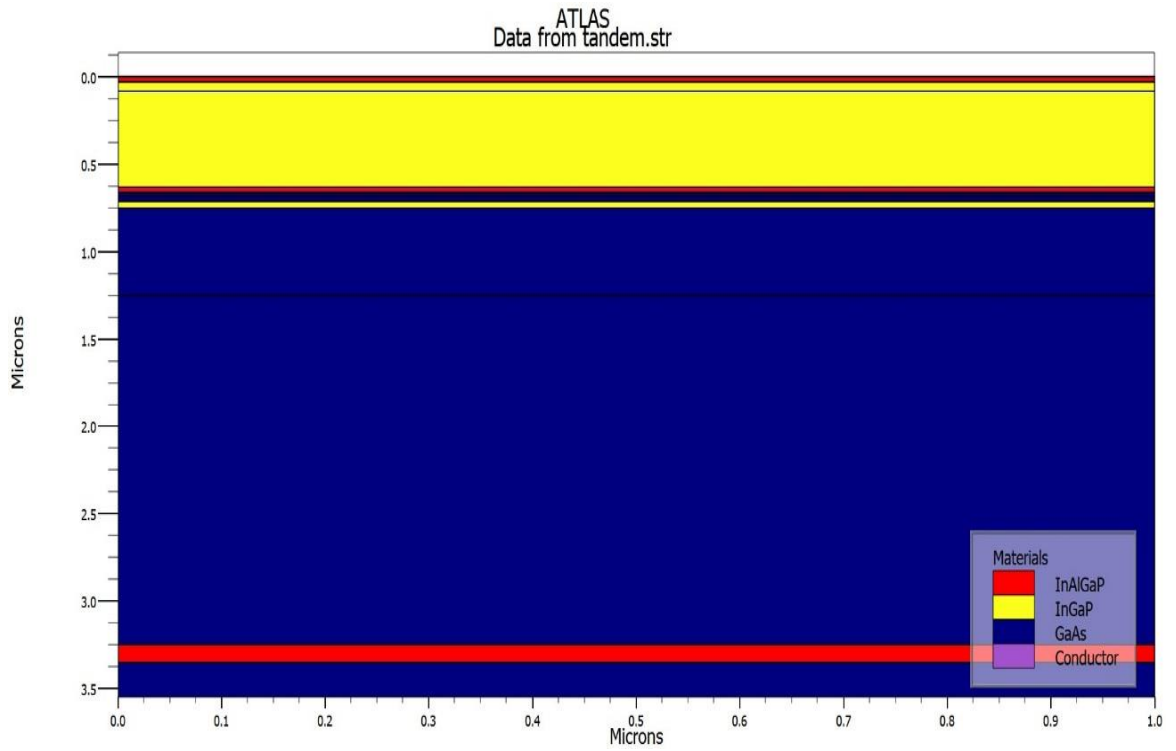
**Fig.(4.17)** Proposed tandem cell structure simulated in ATLAS TCAD.
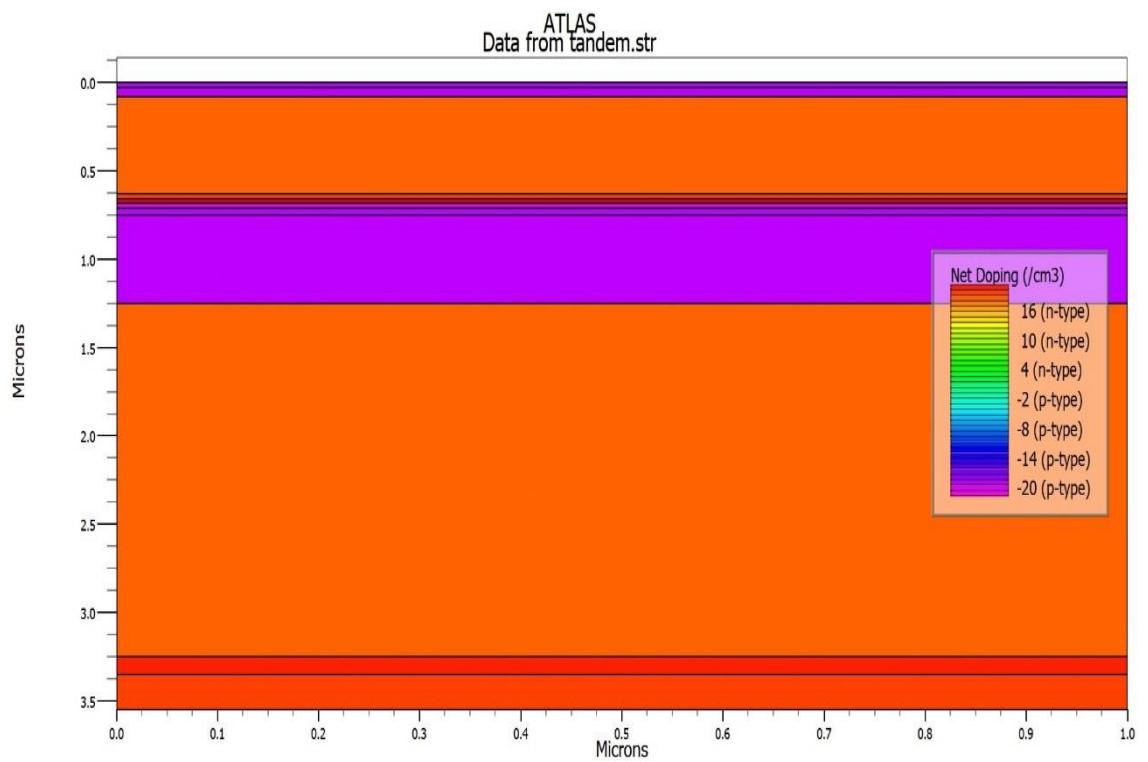


**Fig.(4.18)** Doping profile of the model.

By making a cut line in the tandem cell (InGaP/GaAs), the energy band diagram can be calculated as demonstrated in Fig (4.19).
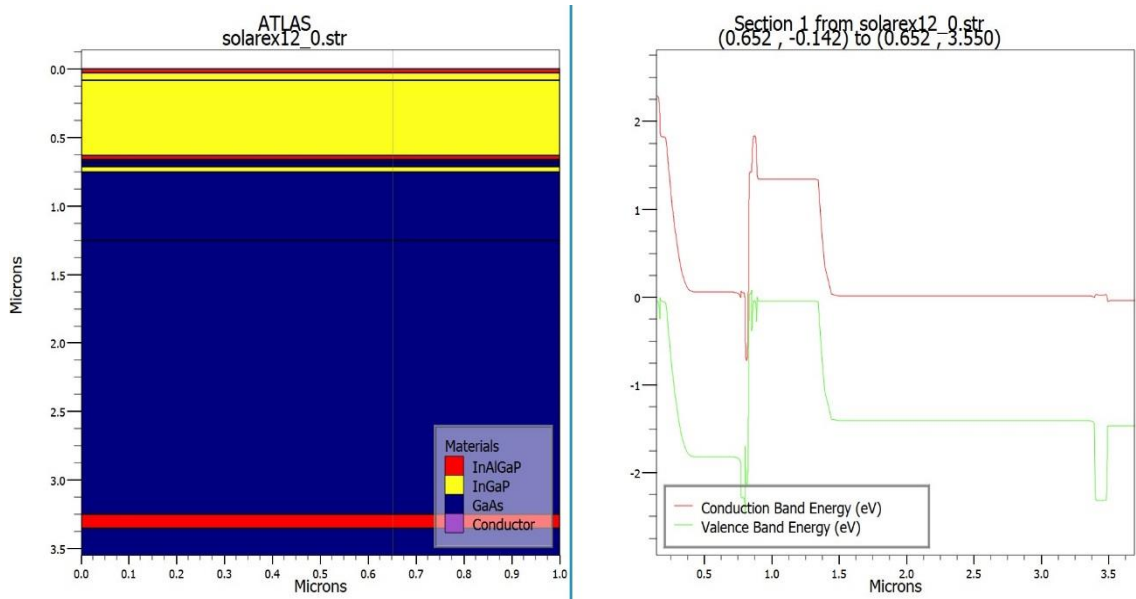


**Fig.(4.19)** The energy band diagram of tandem cell.

The efficiency of the   full tandem cell is equal to 25.10% and the J-V curve is demonstrated in Fig (4.20).
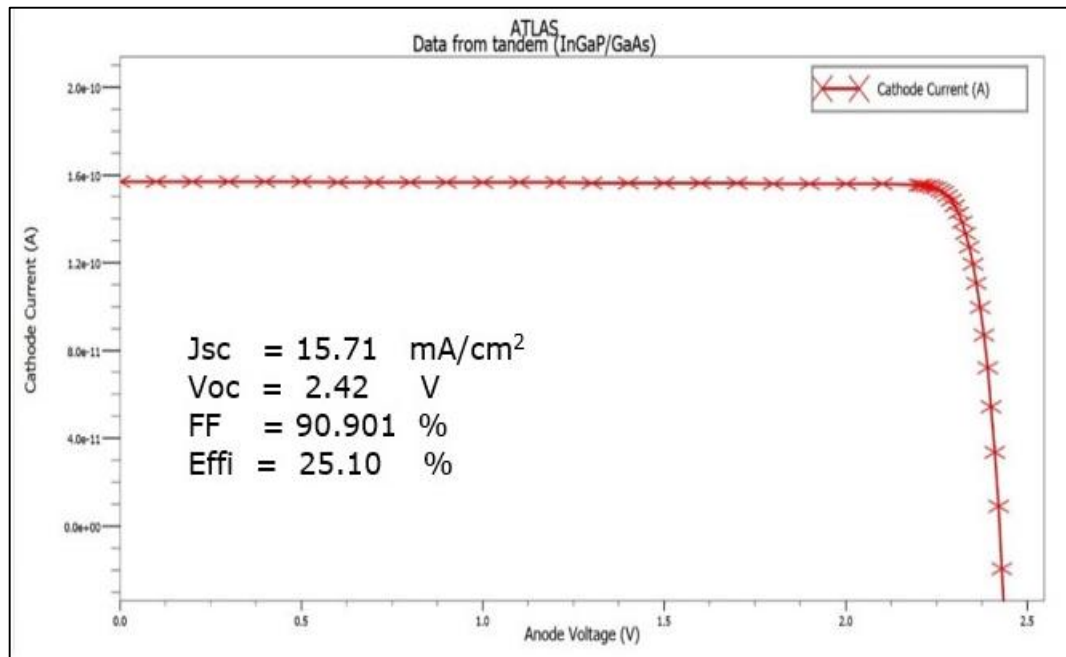


**Fig.(4.20)**  J–V Characteristics of full tandem cell.

## 4.7 The effect of tandem cell parameters on the efficiency of the cell

We varied many parameters to optimize the efficiency InGaP/GaAs tandem cell. Each cell is composed of four distinct layers as illustrated in Fig. (4.14), and each with three independent variables: molar fraction, thickness, and doping concentration.

### 1. The effect of changing the BSF materials thickness of the GaAs lower cell

Major modifications in the main tandem cell parameters can occur via changing the BSF layer thickness of the lower cell

In the upper cell, the BSF layer thickness is 0.03 μm, and in the lower cell the BSF layer thickness is 0.1μm .This layer also has a significant impact on the increasing of solar cell efficiency and increasing short circuit current density as well as avoiding recombination of the carrier. Therefore, the existence of the BSF layer is necessary. Table (4.5) provides a comparison in detail of various properties for two different BSF materials.

**Table (4.5)** Impact of changing the BSF layer thickness of the GaAs lower cell on the significant factors of the tandem cell proposed by using two different BSF materials

| BSF Materials AlGaAs | | | | | BSF Materials InAlGaP | | | | |
|---|---|---|---|---|---|---|---|---|---|
| Thickness (μm) | $J_{SC}$ (mA/cm²) | $V_{OC}$ (V) | FF (%) | Effi (%) | Thickness (μm) | $J_{SC}$ (mA/cm²) | $V_{OC}$ (V) | FF (%) | Effi (%) |
| 0.1 | 14.22 | 2.42 | 91.53 | 22.83 | 0.1 | 15.71 | 2.42 | 90.901 | 25.10 |
| 0.2 | 14.22 | 2.42 | 91.52 | 22.82 | 0.2 | 17.23 | 2.42 | 90.30 | 27.34 |
| 0.3 | 14.22 | 2.42 | 91.52 | 22.82 | 0.3 | 18.68 | 2.42 | 89.35 | 29.34 |
| 0.4 | 14.22 | 2.42 | 91.51 | 22.82 | 0.4 | 20.03 | 2.42 | 87.75 | 30.94 |
| 0.5 | 14.22 | 2.42 | 91.51 | 22.81 | 0.5 | 20.70 | 2.43 | 86.98 | 31.71 |
| 0.6 | 14.21 | 2.42 | 91.50 | 22.81 | 0.6 | 20.70 | 2.43 | 87.69 | 31.99 |
| 0.7 | 14.21 | 2.42 | 91.50 | 22.80 | 0.7 | 20.70 | 2.43 | 87.77 | 32.25 |
| 0.8 | 14.21 | 242 | 91.49 | 22.80 | 0.8 | 20.70 | 2.43 | 88.30 | 32.33 |
| 0.9 | 14.21 | 2.42 | 91.48 | 2280 | 0.9 | 20.70 | 2.43 | 88.47 | 32.39 |
| 1.0 | 14.21 | 2.42 | 91.48 | 22.79 | 1.0 | 20.70 | 2.43 | 88.65 | 32.44 |
| 1.1 | 14.21 | 2.42 | 91.47 | 22.79 | 1.1 | 20.71 | 2.43 | 88.71 | 32.48 |
| 1.2 | 14.20 | 2.42 | 91.47 | 22.79 | 1.2 | 20.71 | 2.43 | 88.79 | 32.52 |
| 1.3 | 14.20 | 2.42 | 91.46 | 22.78 | 1.3 | 20.71 | 2.43 | 88.87 | 32.54 |
| 1.4 | 14.20 | 2.42 | 91.46 | 22.78 | 1.4 | 20.71 | 2.44 | 88.90 | 32.52 |
| 1.5 | 14.20 | 2.42 | 91.45 | 22.77 | 1.5 | 20.71 | 2.44 | 88.89 | 32.58 |
| 1.6 | 14.20 | 2.42 | 91.45 | 22.76 | 1.6 | 20.71 | 2.44 | 88.76 | 32.60 |
| 1.7 | 14.20 | 2.42 | 91.44 | 22.77 | 1.7 | 20.71 | 2.44 | 88.81 | 32.63 |
| 1.8 | 14.20 | 2.42 | 91.44 | 22.76 | 1.8 | 20.71 | 2.44 | 89.10 | 32.65 |
| 1.9 | 14.20 | 2.42 | 91.42 | 22.76 | 1.9 | 20.71 | 2.44 | 89.14 | 32.66 |
| 2.0 | 14.22 | 2.42 | 91.53 | 22.83 | 2.0 | 20.71 | 2.37 | 89.17 | 32.68 |
| 2.1 | 14.20 | 2.42 | 91.41 | 22.76 | 2.1 | 20.71 | 2.25 | 89.19 | 32.70 |

As seen in Table (4.5), it has been found that some parameters are reliant on the thickness of the BSF and also the material employed in this layer. For (InAlGaP) material, increasing BSF thickness for the bottom layer will absorb more photons and increase the output current and approximately saturated at 0.4 μm thickness. The efficiency (η), FF, $J_{SC}$, and $V_{OC}$ of the tandem cell against the BSF thickness of the bottom cell are shown in Fig. (4.21).
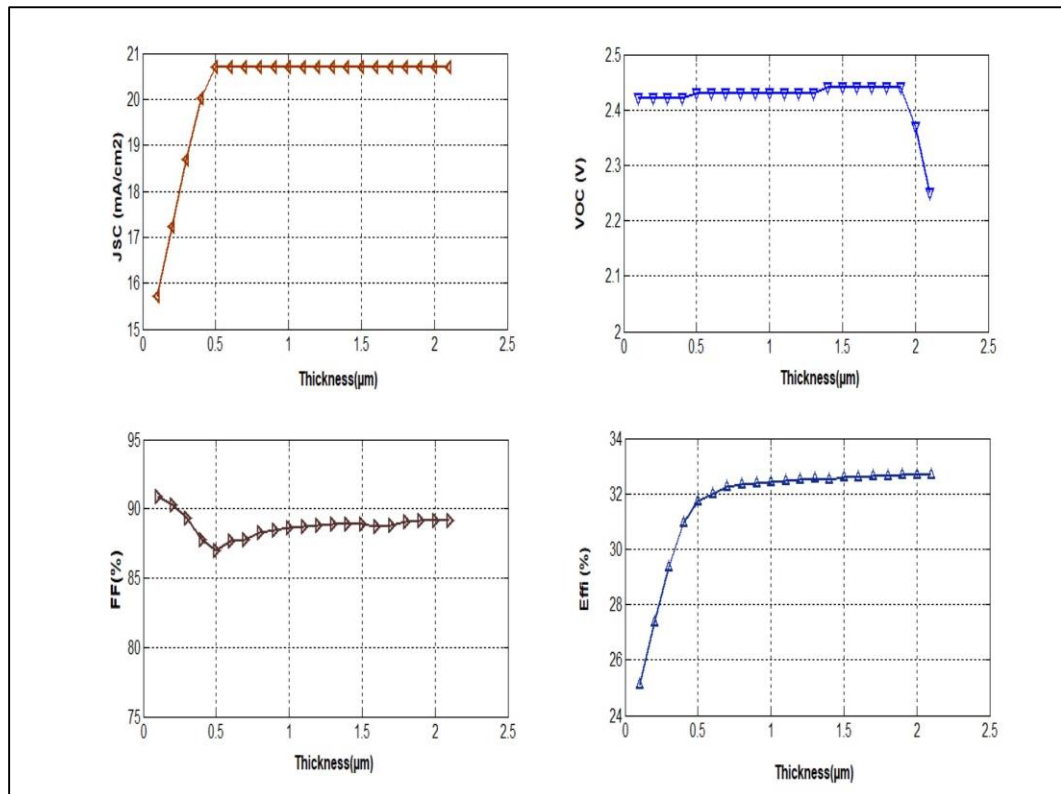
**Fig.(4.21)** The variation effect of (InAlGaP) BSF layer thickness of the bottom cell on the $V_{OC}$, $J_{SC}$, FF and the efficiency

Increasing the thickness for AlGaAs material results in a slight difference value of FF, $J_{SC}$, and efficiency ($\eta$). All of them are almost constant as shown in Table. (4.5). The condition could be due to intrinsic material properties. InAlGaP has a higher absorption coefficient ($\alpha$) than AlGaAs, which results in further photogeneration. (AlGaAs) is a semiconductor material that has a large bandgap of 1.8 eV and has a high sensibility to oxygen and water pollution .For this reason, it is an unfavorable selection for tandem construction.

J–V Characteristics curve generated for the model at thick (BSF) = 2.1µm is shown in Fig. (4.22).



Jsc  = 20.71  mA/cm$^2$
Voc  = 2.44   V
FF   = 89.19  %
Effi = 32.70  %
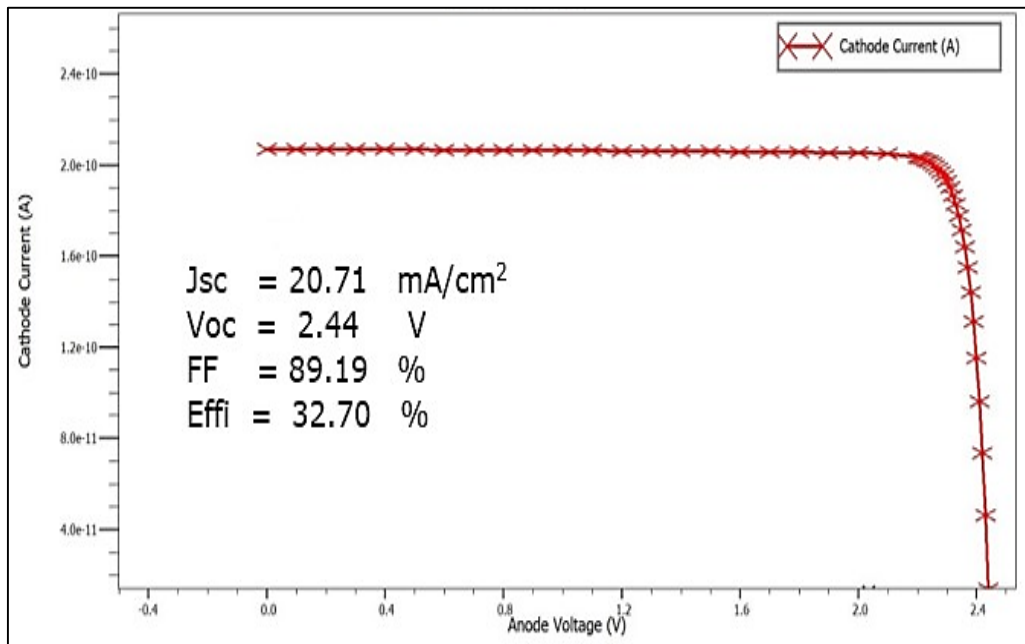
**Fig.(4.22)** J–V Characteristics of tandem cell.

## 2. The impact of changing the thickness and doping concentration of the window layer of the top cell on the tandem cell.

The first layer in a solar cell facing the illumination is the window layer InAlGaP, which is used as a window layer, and the BSF layer that has a wideband gap that allows for the highest absorption in the equipment window layer with a heavily doped region causing a potential barrier between the base region to enclose the minority carriers in the lightly doped region.

To optimize the tandem cell efficiency, the first step is to change the thickness of the window layer from 0.01 µm to 0.06 µm. It is noticed that the tandem cell's efficiency has a maximum value at a thickness of 0.02 µm as shown in Table (4.6). The efficiency was improved from 32.70 % to 33.59%. Fig. (4.24) displays the influence of window thickness on the efficiency of the tandem cells

**Table (4.6)**  Influence of changing window layer width of the InGaP top cell on the significant factors of the tandem cell proposed at doping p=$1\times10^{18}$.

| Thickness (μm) | $J_{SC}$ (mA/cm$^2$) | $V_{OC}$ (V) | FF (%) | Effi (%) |
|---|---|---|---|---|
| 0.01 | 21.35 | 1.48 | 75.80 | 17.38 |
| 0.02 | 21.20 | 2.45 | 89.31 | 33.59 |
| 0.03 | 20.6 | 2.25 | 89.19 | 32.70 |
| 0.04 | 20.03 | 2.44 | 45.88 | 16.41 |
| 0.05 | 20.70 | 1.48 | 75.78 | 16.12 |
| 0.06 | 20.17 | 1.48 | 75.75 | 15.85 |
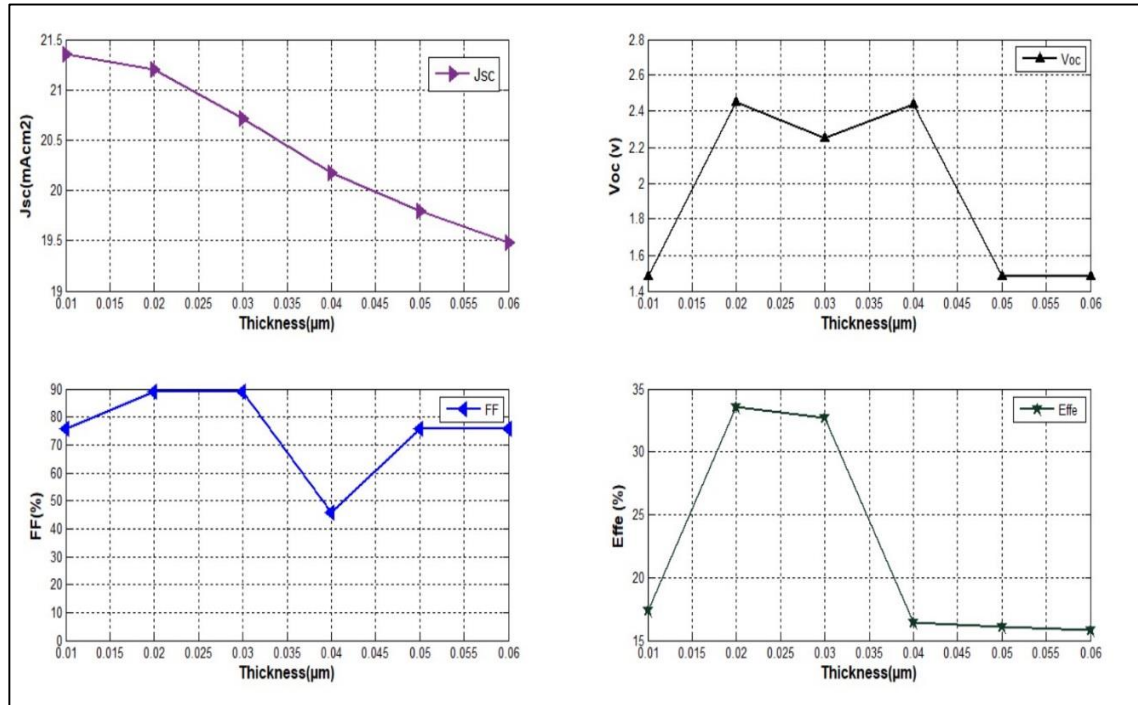


**Fig.(4.23)** The variation effect of window layer thickness on the $V_{OC}$, $J_{SC}$, FF and η.

The second step is to change the doping concentration of the window layer from $N_a= 2\times10^{18}$ cm$^{-3}$ to $N_a= 1\times10^{18}$ cm$^{-3}$, reducing doping concentration leads to an enhancement in the efficiency and makes it equal to 34.24 %.  It is found that the efficiency is maximum at 0.02 μm thickness of the top cell. Fig. (4.25) illustrates the impact of variation of the window layer doping concentration versus $V_{OC}$, $J_{SC}$, FF and efficiency.μ
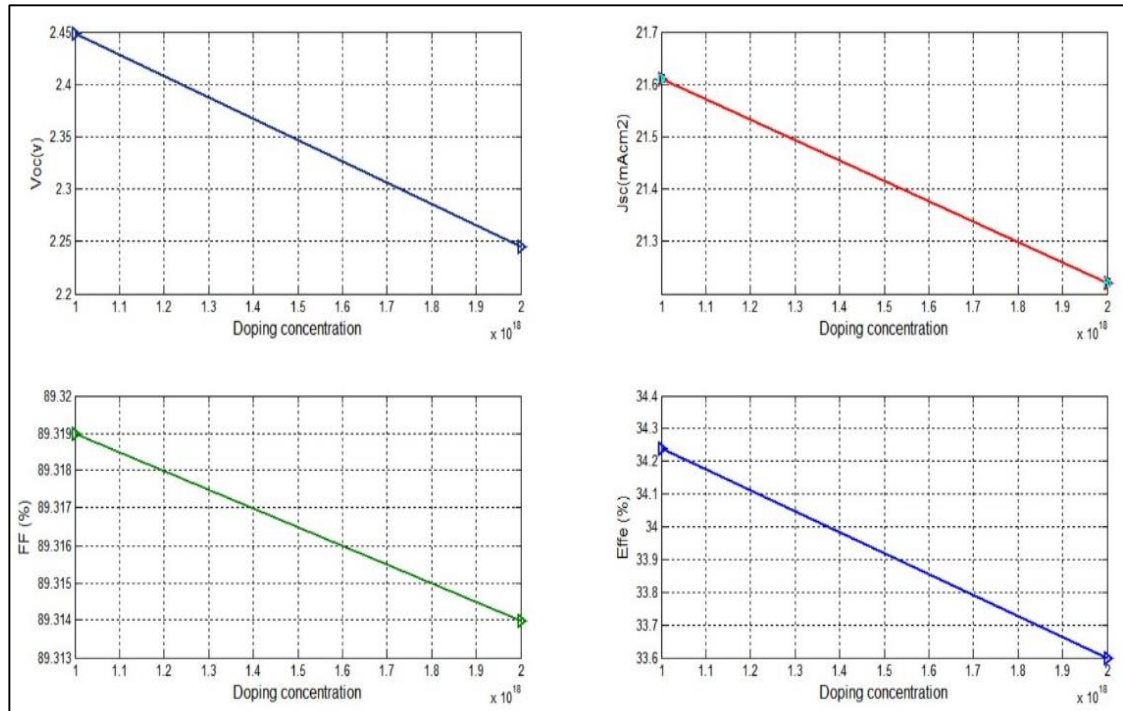
**Fig.(4.24)** The window layer doping concentration variation effect on the $V_{OC}$, $J_{SC}$, FF and η.

### 3. The effect of changing the tunnel junction materials:

GaAs is utilized as a tunnel junction since it has lower optical absorption and lowers series resistance trajectory which decreases the length of the depletion region so that the electrons can effectively tunnel through it. Table (4.7) illustrates the tandem cell efficiency with the tunnel junction materials change. The tunneling performance of the InGaP/GaAs tunnel diode appears to be better than GaAs/GaAs because it generates a greater tunneling current. Furthermore, InGaP has higher transparency from GaAs because of its wide bandgap, which enhances device efficiency slightly as shown in Table (4.7).

**Table (4.7)** The impact of changing the tunnel junction materials on the suggested tandem cell characteristics.

| TJ materials | $J_{SC}$ (mA/cm$^2$) | $V_{OC}$ (V) | FF (%) | Effi (%) |
|---|---|---|---|---|
| GaAs/GaAs | 21.614 | 2.448 | 89.31 | 34.24 |
| InGaP/GaAs | 21.690 | 2.449 | 89.33 | 34.37 |

## 4.8 The optimum structure of the tandem cell (InGaP/GaAs)

The optimal structure of (InGaP/GaAs) tandem cell has produced an efficiency of 34.37%, $V_{OC}$ of 2.449V, $J_{SC}$ of 21.69 mA/cm$^2$, fill factor of 89.33 % that optimized its input parameters produced from previous parameters study as demonstrated in the schematic diagram Fig. (4.25).

| | | | |
|---|---|---|---|
| **Anode Contact** | | | |
| 0.02 µm | window | $In_{0.5}(Al_{0.7}Ga_{0.3})_{0.5}P$ | $P = 1e18$ cm$^{-3}$ |
| 0.05 µm | Emitter | $In_{0.49}Ga_{0.5\,1}P$ | $P = 2e18$ cm$^{-3}$ |
| 0.55 µm | Base | $In_{0.49}Ga_{0.5\,1}P$ | $n = 7e16$ cm$^{-3}$ |
| 0.03 µm | BSF | $In_{0.5}(Al_{0.7}Ga_{0.3})_{0.5}P$ | $n = 2e18$ cm$^{-3}$ |
| 0.025 µm | Tunnel Diode | GaAs | $n = 5e19$ cm$^{-3}$ |
| 0.025 µm | Tunnel Diode | $In_{0.49}Ga_{0.5\,1}P$ | $P = 3e19$ cm$^{-3}$ |
| 0.04 µm | window | $In_{0.49}Ga_{0.5\,1}P$ | $P = 3e18$ cm$^{-3}$ |
| 0.50 µm | Emitter | GaAs | $P = 2e18$ cm$^{-3}$ |
| 2.00 µm | Base | GaAs | $n = 2e17$ cm$^{-3}$ |
| 2.10 µm | BSF | $In_{0.5}(Al_{0.7}Ga_{0.3})_{0.5}P$ | $n = 5e18$ cm$^{-3}$ |
| 0.20 µm | Substrate | GaAs | $n = 1e18$ cm$^{-3}$ |
| **Cathode Contact** | | | |

**Fig.(4.25)** The Final schematic diagram of the tandem cell.

The structure of the energy band, the J-V curve, and the external quantum efficiency of the optimum tandem cell are illustrated in figures. (4.26), (4.27), and (4.28) respectively.
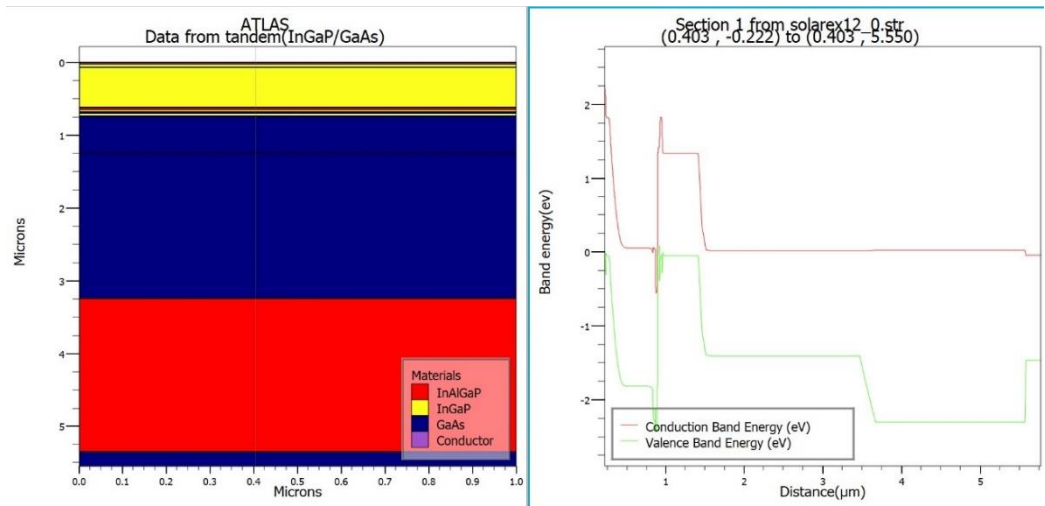
**Fig.(4.26)** The energy band diagram of tandem cell.



Jsc  = 21.69  mA/cm²
Voc = 2.449  V
FF   = 89.33  %
Effi = 34.37  %
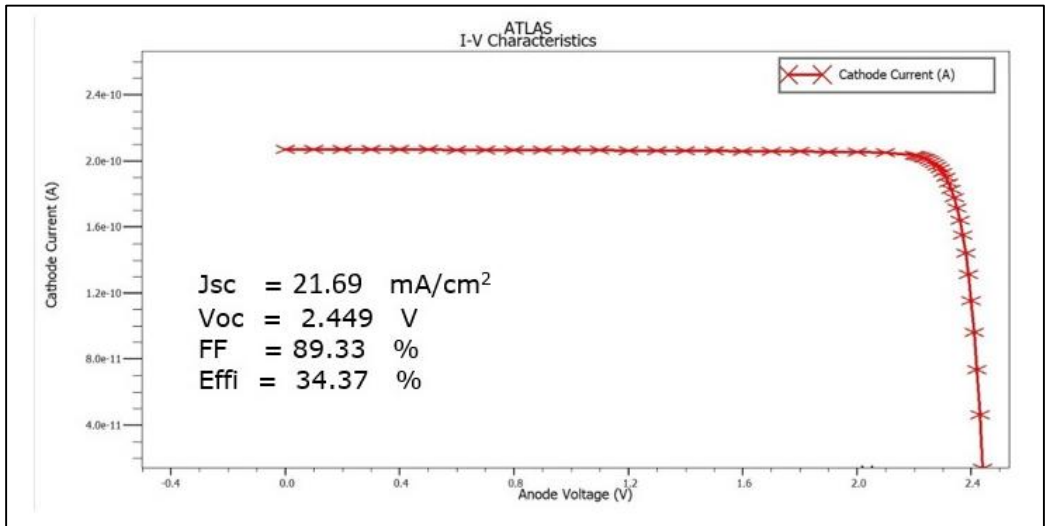
**Fig.(4.27)** The J–V Characteristics of final tandem cell.
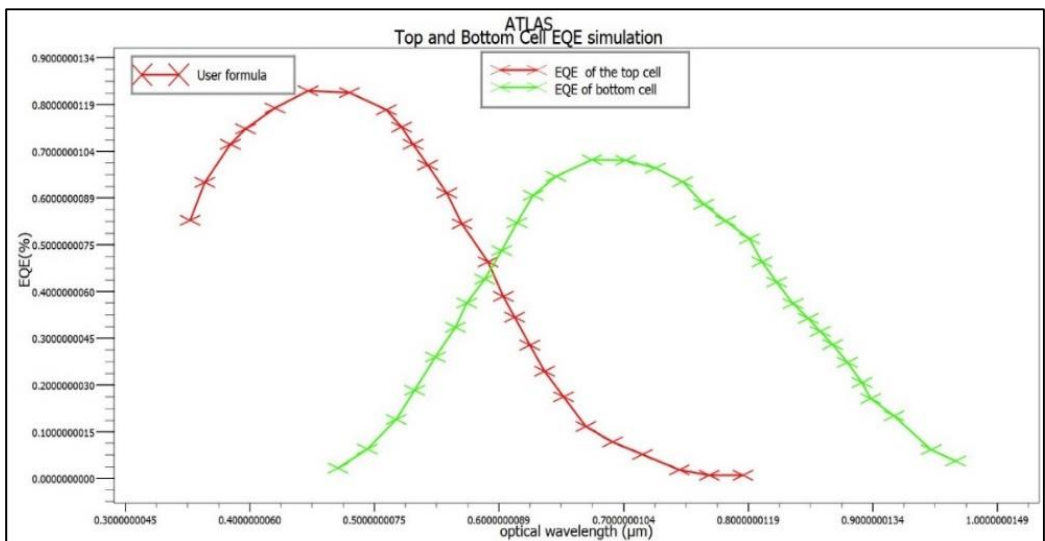


**Fig.(4.28)** EQE of the upper and lower cells.

The electrical field has a maximum value in the tunnel area as demonstrated in Fig. (4.29). This happened because of the potential that was built-in inside the junction area.
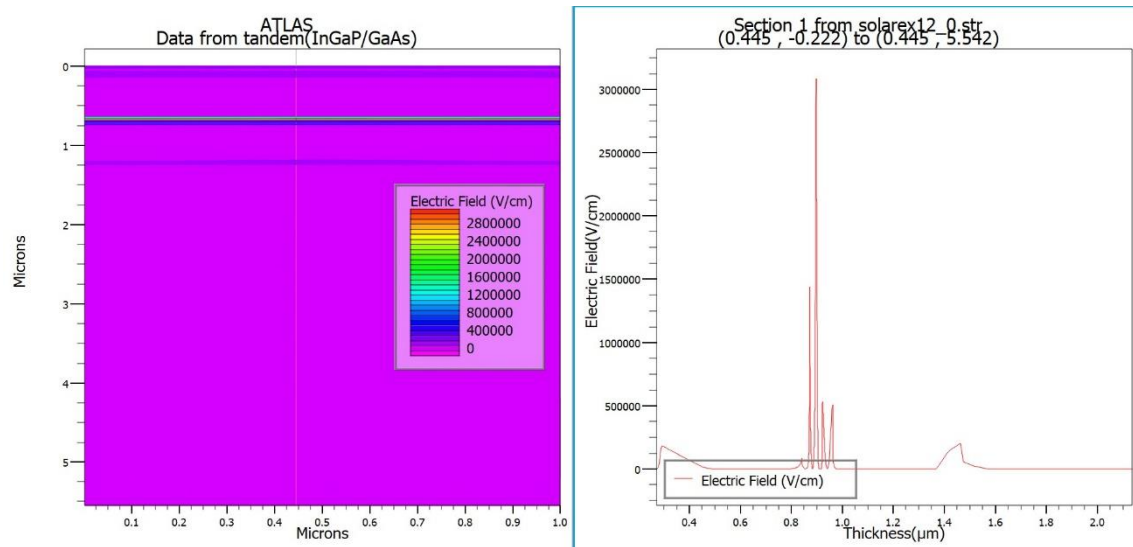


**Fig.(4.29)** The advanced electric field in various layers.

As known, the voltage of tandem cell is equal to the sum of the voltage in two single cell models which accounts for the voltage release across a tunnel junction.

In Fig. (4.30), the potential advance in every layer of the cell is visibly shown. In ideal case, the two cells will produce an identical current similar to a single cell and the achieved current in the tandem cell will be smaller than the two due to the high energy photons absorbed in the top cell (InGaP), and the lower cell cannot generate many of EHPs and for this reason, achieves a small current compared to the ideal case. So, there shall be a large potential across the junction region.
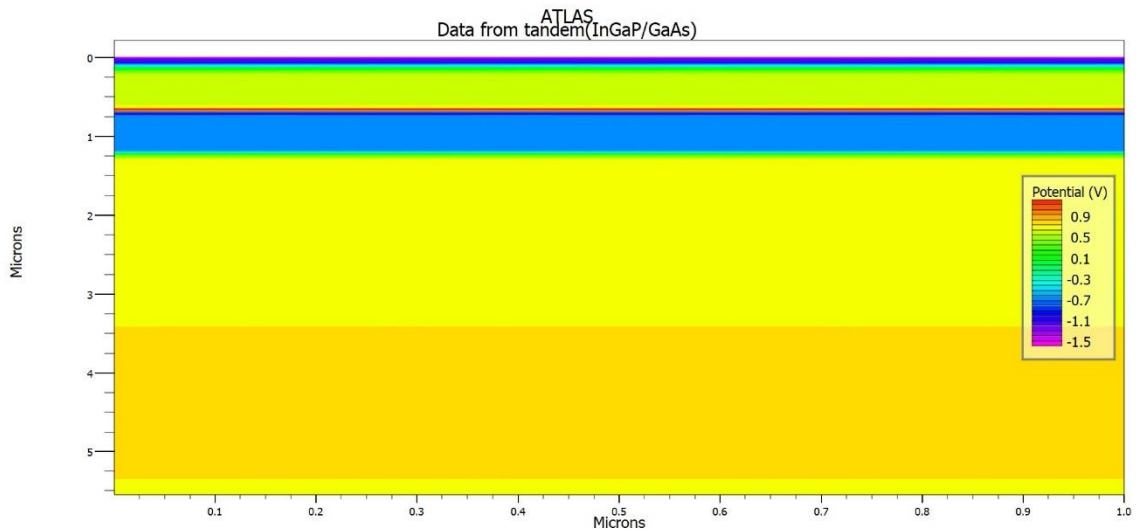
**Fig.(4.30)** The electric potential in various layers of tandem cell.

Essential parameters of the plots of the three cells are summarized in Table (4.8).

**Table (4.8)** The essential parameters of the three designed cells

| parameter | Upper Cell (0.65um) | Lower cell (4.84um) | Tandem Cell (5.54 um) |
|---|---|---|---|
| **Voc (V)** | 1.403 | 1.0050 | 2.449 |
| **Jsc (mA/cm$^2$)** | 19.70 | 35.74 | 21.69 |
| **FF (%)** | 85.65 | 88.64 | 89.33 |
| **Effi(%)** | 17.15 | 23.071 | 34.37 |

Finally, a comparison between main parameters of the proposed tandem structure with other works is exhibited in Table (4.9).

**Table (4.9)** Comparison between the proposed structures with other works.

| tandem cells | Jsc (mA/cm$^{-2}$) | Voc (V) | FF (%) | Effi(%) |
|---|---|---|---|---|
| InGaP/GaAs[23] | 10.9 | 2.32 | 79.00 | 23.6 |
| InGaP/GaAs[25] | 10.66 | 2.34 | 87.84 | 25.78 |
| InGaP/GaAs[29] | 19.853 | 2.483 | 89.473 | 32.593 |
| **Proposed design** | 21.69 | 2.449 | 89.33 | 34.37 |

It has been noticed that the obtained efficiency is better compared to the literature.

## 4.9 Effect of Temperature on the optimal tandem cell

Existing literature shows that semiconductors are usually modeled at a room temperature of 300K. Solar cells are responsive to temperatures just like other semiconductor devices.

The gap in the semiconductor band is reduced due to an increase in temperature as a result of increasing the energy of electrons in the material.

The tandem cells were simulated at 300, 325,..., 400 K.Table (4.10) displays the outcomes of this simulation. These results show that the efficiency decreases by about 8 % for each (25-K) increment in temperature. Temperature also influences the band gap of the materials.

Within actuality, as the temperature rises above 300 K, the bandgap narrows. Equation of Varshni demonstrates how the bandgap various due to the temperature[84].

$$E_g = E_{g(300K)} + \alpha \left[ \frac{(300K)^2}{(300K) + \beta} - \frac{T^2}{T + \beta} \right] \qquad (4.4)$$

where, $E_{g(300K)}$ is the bandgap of the material at (300 K ), and "α" and "β" are empirically determined values that are defined for each semiconductor material. Table (4.10) indicates the impact of temperature changes on key parameters of the optimum structure.

Table **(4.10)** Effect of temperature change on the optimum solar cell performance.

| Temperature (K) | $J_{SC}$ (mA/cm$^2$) | $V_{OC}$ (V) | FF (%) | Effi (%) |
|---|---|---|---|---|
| 300 | 21.69 | 2.44 | 89.33 | 34.37 |
| 325 | 21.64 | 2.35 | 87.55 | 32.30 |
| 350 | 21. 61 | 2.24 | 86.69 | 31.50 |
| 375 | 21.53 | 2.14 | 86.47 | 28.87 |
| 400 | 21.43 | 2.05 | 85.20 | 27.21 |

The effect of temperature increases on optimum structure efficiency, open-circuit voltage, fill factor, and short circuit density is reflected in Fig. (4.31).
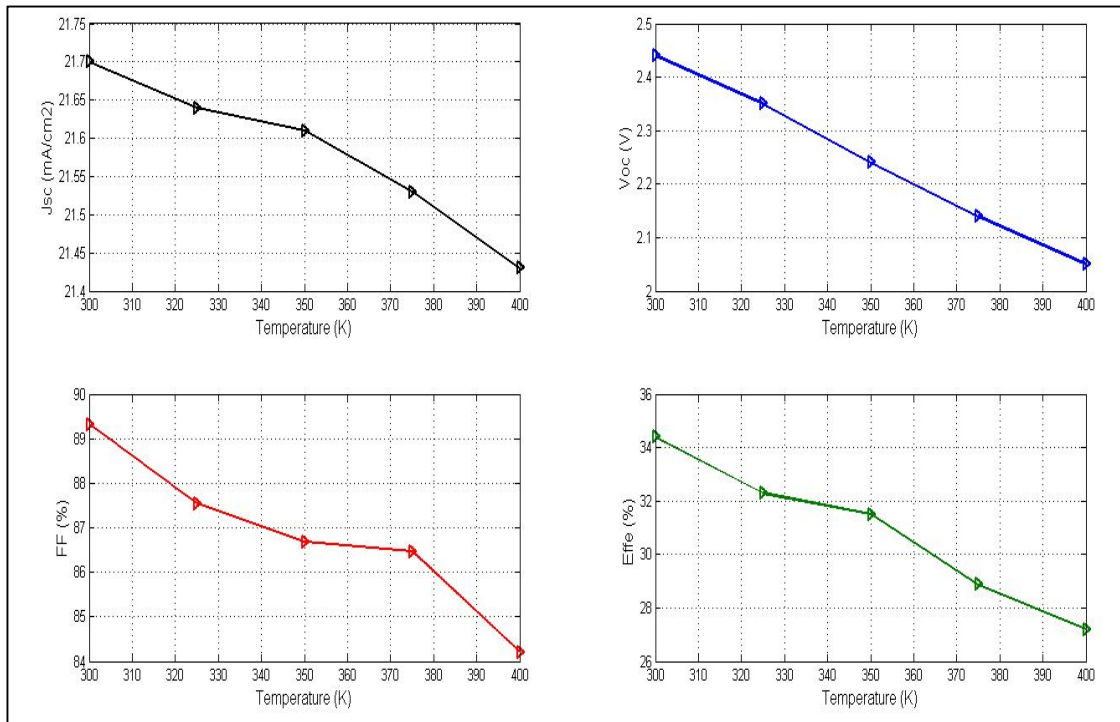


**Fig.(4.31)** The effect of temperature change on Important Parameters of the optimum structure.

As observed from Fig (4.31), the efficiency of the solar cell decreases with increasing values temperature. The FF also decreases because of the significant decrease in $V_{OC}$. The decrease in $V_{OC}$ leads to a decreased conversion efficiency of the solar cell.

# CHAPTER FIVE

## CONCLUSION AND FUTURE WORK

### 5.1 Conclusions

In the present work, a multi-layer solar cell (tandem) solar cell was subjected to a step-by-step improvement study. Cells were divided into an InGaP and a GaAs and each subcell was numerically simulated. And a complete tandem has been obtained from the simulated top and bottom subcells. This work illustrates several suggested tandem cell characteristics, like efficiency ($\eta$), fill factor (FF), external quantum efficiency (EQE), open-circuit voltage ($V_{OC}$), and short circuit current density ($J_{SC}$).

1. The optimization process was performed by adjusting the bandgap of the top cell, increasing the thickness of BSF of the bottom cell, modifying the doping concentration, the thickness of the window layer of the top cell, and changing the tunnel junction material.

2. The results show that increasing the thickness of BSF will lead to an increase in the short circuit current density ($J_{SC}$) and also the suggested cell performance efficiency was increased.

3. The results show that in case of a decrease in the thickness of the window layers, the efficiency is improved. The tandem demonstrates a good improvement in significant properties of the solar cell because more transparency is created in the junction of the tunnel, and more collection of carriers happens.

4. The obtained results from the optimal dual junction cell structure are, (Jsc) of (21.69 mA/cm$^2$), and ($V_{OC}$) is (2.449 V), (FF) is (89.33%), and ($\eta$) is about (34.37%).

5. The effect of temperature was studied from 300 K to 400 K and it is observed that the cell performance decreased when the temperature increased.

## 5.2 Future work

Further research must concentrate on three fields.

1.  Thickness improvement of each layer to achieve higher efficiency

2.  Improving the molar fraction composition, the tandem cell design can especially be optimized.

3. Optimizing the doping concentration or thickness of the tunnel junction.

# References

[1] A. E. Becquerel, "On electric effects under the influence of solar radiation," *CR Acad. Sci*, vol. 9, pp. 711–714, 1839.

[2] D. M. Chapin, C. S. Fuller, and G. L. Pearson, "A new silicon p-n junction photocell for converting solar radiation into electrical power," *J. Appl. Phys.*, vol. 25, no. 5, pp. 676–677, 1954.

[3] W. Shockley and H. J. Queisser, "Detailed balance limit of efficiency of p-n junction solar cells," *J. Appl. Phys.*, vol. 32, no. 3, pp. 510–519, 1961.

[4] N. V Yastrebova, "High-efficiency multi-junction solar cells: Current status and future potential," *Cent. Res. Photonics, Univ. Ottawa*, p. 17, 2007.

[5] Y. H. Zhang, S. N. Wu, D. Ding, S. Q. Yu, and S. R. Johnson, "A proposal of monolithicly integrated multijunction solar cells using lattice-matched II/VI and III/V semiconductors," in *33rd IEEE Photovoltaic Specialists Conference*, 2008, pp. 1–5.

[6] D. Friedman, "Progress and challenges for next-generation high-efficiency multijunction solar cells," *Curr. Opin. Solid State Mater. Sci.*, vol. 14, no. 6, pp. 131–138, 2010.

[7] A. Gnilenko and S. Plaksin, "Mechanically Stacked Triple-junction GaInP/GaAs/Si Solar Cell Simulation," *J. Nano-and Electron. Phys.*, vol. 5, no. 4, pp. 4057–1, 2013.

[8] M. S. Leite *et al.*, "Towards an optimized all lattice-matched InAlAs/InGaAsP/InGaAs multijunction solar cell with efficiency >50%," *Appl. Phys. Lett.*, vol. 102, no. 3, 2013.

[9] M. Stan *et al.*, "Very high efficiency triple junction solar cells grown by MOVPE," *J. Cryst. Growth*, vol. 310, no. 23, pp. 5204–5208, 2008.

[10] M. Yamaguchi, "Multi-junction solar cells and novel structures for solar cell applications," *Phys. E Low-Dimensional Syst. Nanostructures*, vol. 14, no. 1–2, pp. 84–90, 2002.

[11] M. Hermle, G. Letay, S. Philipps, and A. W. Bett, "Numerical simulation of tunnel diodes for multi-junction solar cells," *Prog. Photovoltaics Res. Appl.*, vol. 16, no. 5, pp. 409–418, 2008.

[12] K. K. Mohammed, "High Efficiency Tandem Solar Cell based on InGaP and GaAs for Sustainable Energy Applications," *Int. J. Comput. Appl.*, vol. 181, no. 18, pp. 26–30, 2018.

[13] N. Amin, M. Tang, and K. Sopian, "Numerical modeling of the copper-indium-selenium (CIS) based solar cell performance by AMPS-1D,"

in *5th Student Conference on Research and Development, SCORED*, 2007, pp. 1–6.

[14] A. Blakers, N. Zin, K. R. McIntosh, and K. Fong, "High efficiency silicon solar cells," *Energy Procedia*, vol. 33, pp. 1–10, 2013.

[15] E. Jackson, "Areas for improvement of the semiconductor solar energy converter," *Trans. Intern. Conf. Use Sol. Energy*, vol. 5, p. 122, 1955.

[16] M. Wolf, "Limitations and Possibilities for Improvement of Photovoltaic Solar Energy Converters: Part I: Considerations for Earth's Surface Operation," *Proc. IRE*, vol. 48, no. 7, pp. 1246–1263, 1960.

[17] J. C. Fan, B.-Y. Tsaur, and B. Palm, "Optimal design of high-efficiency tandem cells," in *16th Photovoltaic Specialists Conference*, 1982, pp. 692–701.

[18] J. Hutchby, R. Markunas, M. Timmons, P. Chiang, and S. Bedair, "A review of multijunction concentrator solar cells," in *Conference Record of the IEEE Photovoltaic Specialists Conference*, 1985, pp. 20–27.

[19] B.-C. Chung, G. Virshup, S. Hikido, and N. Kaminar, "27.6% Efficiency (1 sun, air mass 1.5) monolithic Al0.37Ga 0.63As/GaAs two-junction cascade solar cell with prismatic cover glass," *Appl. Phys. Lett.*, vol. 55, no. 17, pp. 1741–1743, 1989.

[20] B. Garcia Jr, "Indium gallium nitride multijunction solar cell simulation using silvaco atlas," 2007.

[21] N. Shigekawa, M. Morimoto, S. Nishida, and J. Liang, "Surface-activated-bonding-based InGaP-on-Si double-junction cells," *J. Appl. Phys.*, vol. 53, no. 45, p. 04ER05, 2014.

[22] M. Yamaguchi, "Radiation-resistant solar cells for space use," vol. 68, pp. 31–53, 2001.

[23] M. Lueck, C. Andre, A. Pitera, M. Lee, E. Fitzgerald, and S. Ringel, "Dual junction GaInP/GaAs solar cells grown on metamorphic SiGe/Si substrates with high open circuit voltage," *IEEE Electron Device Lett. 27*, vol. 27, no. 3, pp. 142–144, 2006.

[24] B. D. M. FILLALI, M. Fillali, and B. Dennai, "IMPACT OF TUNNEL HETEROJUNCTION (InGaP/GaA) DOPING CONCENTRTION ON THE PERFORMANCE OF InGaP/GaAs TONDEM SOLAR CELL USING SILVACO-ATLAS SOFTWARE," *J. Ovonic Res.*, vol. 15, no. 5, pp. 279–285, 2019.

[25] J. Leem, Y. Lee, and J. Yu, "Optimum design of InGaP/GaAs dual-junction solar cells with different tunnel diodes," *Opt. Quantum*

*Electron.*, vol. 41, no. 8, pp. 605–612, 2009.

[26] S. J. Wojtczuk, S. M. Vernon, and M. M. Sanfacon, "Comparison of windows for P-on-N InGaP solar cells," in *Conference Record of the Twenty Third IEEE Photovoltaic Specialists Conference*, 1993, pp. 655–658.

[27] J. Olson, S. Kurtz, A. Kibbler, and P. Faine, "A 27.3% efficient Ga0.5In0.5P/GaAs tandem solar cell," *Appl. Phys. Lett.*, vol. 56, no. 7, pp. 623–625, 1990.

[28] F. P. M. benaicha, L. Dehimi, f. Bouzid, M. Benaicha, L. Dehimi, F. Pezzimenti, and F. Bouzid, "Simulation Analysis of a high efficiency GaInP/Si multijunction solar cell," *J. Semicond.*, vol. 41, no. 3, p. 032701, 2020.

[29] M. H. Tsutagawa and S. Michael, "Triple junction InGaP/GaAS/Ge solar cell optimization: The design parameters for a 36.2\% efficient space cell using Silvaco ATLAS modeling \& simulation," in *34th IEEE Photovoltaic Specialists Conference (PVSC)*, 2009, pp. 001954–001957.

[30] B. G. Streetman, S. Banerjee, and Others, *Solid state electronic devices*, vol. 10. 2009.

[31] M. Lundstrom, "Introduction to Photovoltaics," *Cl. notes NCN Summer Sch. Purdue Univ. West Lafayette, IN, USA*, 2011.

[32] B. Acar, "A numerical analysis of interdigitated back contacted silicon solar cells," Middle East Technical University, 2018.

[33] A. M. Al-Rjoub, "Design, fabrication, characterization and aging studies of solar selective absorber surfaces," no. March, 2019.

[34] S. Roerink, "Development of a-SiGe: H: from material characterization to multi-junction device," 2019.

[35] "Color wavelength table," 2007. http://www.usbyte.com/common/approximate_wavelength.htm.

[36] B. Ashish, "Optimizing the p-contact of nip substrate solar cell for multi-junction device," Delft University of Technology, 2019.

[37] Y. H. Khattak, Yousaf HameedKhattak, "Modeling of high power conversion efficiency thin film solar cells," Universitat Polit`ecnica de Val`encia, 2019.

[38] A.-M. Mandong, "Design and simulation of single, double, and multi-layer antireflection coating for crystalline silicon solar cell," Karadeniz Teknik, 2019.

[39] S. Michael, "Space power and Radiation Effects," Naval Postgraduate

School, 2009.

[40] O. O. Ogbomo, E. H. Amalu, N. Ekere, and P. Olagbegi, "A review of photovoltaic module technologies for increased performance in tropical climate," *Renew. Sustain. Energy Rev.*, vol. 75, pp. 1225–1238, 2017.

[41] A. H. Smets, K. Jäger, O. Isabella, R. A. Swaaij, and M. Zeman, "Solar Energy: The physics and engineering of photovoltaic conversion, technologies and systems," *Technol. Syst.*, p. 3, 2016.

[42] S. S. Li, *Semiconductor physical electronics*. Springer Science & Business Media, 2012.

[43] A. Goetzberger, J. Knobloch, and B. Voss, *Crystalline silicon solar cells*. Wiley Online Library, 1998.

[44] G. S. Sahoo and G. P. Mishra, "Effect of wideband gap tunnel diode and thickness of the window layer on the performance of a dual junction solar cell," *Procedia Technol.*, vol. 25, pp. 684–691, 2016.

[45] O. Isabella, A. H. Smets, and M. Zeman, "Solar energy: fundamentals, technology, and systems," pp. 83–98, 2014.

[46] Alireza Soheili, Mohsen Hayati and F. Shama, "An optimized efficient double junction CGS/CIGS solar cell with improved performance," *Optik (Stuttg).*, vol. 222, no. 165461, 2020.

[47] W. J. Lee, "Investigation of thin-film CdTel/Ge tandem solar cells," The University of Western Australia, 2017.

[48] S. Gatz, T. Dullweber, and R. Brendel, "Evaluation of series resistance losses in screen-printed solar cells with local rear contacts," *IEEE J. Photovoltaics*, vol. 1, no. 1, pp. 37–42, 2011.

[49] M. A. Green, "Solar cells: operating principles, technology, and system applications," *Englewood Cliffs*, 1982.

[50] M. Wiering, "New Methods of Texturing Crystalline Silicon For Multi-Junction Solar Cell Applications," 2020.

[51] S. Lansel, "Technology and future of III-V multi-junction solar cells," *Int. J. Appl. Phys*, vol. 6, no. 3, pp. 3–8, 2010.

[52] GS Sahoo, G. P. Mishra, and G. Sahoo, GS and Mishra, "Efficient use of low-bandgap GaAs/GaSb to convert more than 50% of solar radiation into electrical energy: a numerical approach," *J. Electron. Mater.*, vol. 48, no. 1, pp. 560–570, 2019.

[53] G. C. Enebe, "Modeling and Simulation of Nanostructured Copper Oxides Solar Cells for Photovoltaic Application," University of Johannesburg (South Africa), 2019.

[54] Faruk KÜRKER, "Microfabrication Based Design and Simulation of Heterojunction Solar Cell," Cukurova University Institute of Natural and Applied Sciences, 2010.

[55] S.-Y. Chang, "Achieving High Efficiency Organic Solar Cells by Device Structure Engineering," University of California, Los Angeles, 2019.

[56] S. Chowdhury, "Design and optimization of an InGaP/GaAs/SixGe1-x solar cell considering recombination effects," 2015.

[57] P. S. Priambodo, N. R. Poespawati, and D. Hartanto, *Solar Cells - Silicon Wafer-Based Technologies*. 2011.

[58] J. S. Walsh, "Optimization of Multi-Junction Solar Cells for Space Applications Modeled With Silvaco Atlas," 2018.

[59] J. Dutta, P. Nayak, and G. Mishra, "Design and evaluation of ARC less InGaP/GaAs DJ solar cell with InGaP tunnel junction and optimized double top BSF layer," *Optik (Stuttg).*, vol. 127, no. 8, pp. 4156–4161, 2016.

[60] S. Sze and K. Ng, "p-n junction," *Phys. Semicond. Devices*, vol. 2, pp. 80–89, 2006.

[61] P. Nayak, J. Dutta, G. P. Mishra, J. D. PP Nayak, and G. P. Mishra, "Efficient InGaP/GaAs DJ solar cell with double back surface field layer," *Eng. Sci. Technol. an Int. J.*, vol. 18, no. 3, pp. 325–335, 2015.

[62] J. Verma, P. Dey, A. Prajapati, and T. Das, "Multi BSF layer InGaP/GaAs high efficiency solar cell," in *2017 11th International Conference on Intelligent Systems and Control (ISCO)*, 2017, pp. 278–281.

[63] H. R. Arzbin and A. Ghadimi, "Improving the performance of a multi-junction solar cell by optimizing BSF, base and emitter layers," *Mater. Sci. Eng. B*, vol. 243, pp. 108–114, 2019.

[64] J. Utsler, "Genetic algorithm based optimization of advanced solar cell designs modeled in Silvaco AtlasTM," Citeseer, 2006.

[65] D. A. Kliner, "A Versatile , Next - Generation Fiber Laser Platform for kW Materials Processing," in *84th Laser Materials Processing Conference*, 2016, pp. 1–7.

[66] A. Bouhdjar, "Study and numerical simulation of (a-Si:H/uc-Si:H) hetrojunction solar cell," Universite' Mohamed Khider-Biskra, 2016.

[67] M. Fillali, B. Dennai, and A. Gani, "Contribution of the Doping of the Lower Window Layer to Improve the Performances of the Tandem Solar Cell," *Alger. J. Renew. Energy Sustain. Dev.*, vol. 01, no. 02, pp.

136–143, 2019.

[68] C. Santa Clara, *ATLAS User's Manual*, Vols. 1-2. 2012.

[69] A. Narasimha, Shreesh and Rohatgi, Ajeet and Weeber, S. Narasimha, A. Rohatgi, and A. Weeber, "An optimized rapid aluminum back surface field technique for silicon solar cells," *IEEE Trans. Electron Devices*, vol. 46, no. 7, pp. 1363–1370, 1999.

[70] Silvaco, "Atlas User 's Manual: Device Simulation Software," *St. Clara, CA*, no. 408, pp. 567–1000, 2014.

[71] Ahmed Benlekhdim, Ali Cheknane, Larbi Sfaxi and H. S. Hilal, "Efficiency improvement of single-junction InGaP solar cells by advanced photovoltaic device modeling," *Optik (Stuttg).*, vol. 163, pp. 8–15, 2018.

[72] I. Vurgaftman, J. Meyer, and L. 'aR Ram-Mohan, "Band parameters for III--V compound semiconductors and their alloys," *J. Appl. Phys.*, vol. 89, no. 11, pp. 5815–5875, 2001.

[73] Shin-ichiro Sato, Haruki Miyamoto, Mitsuru Imaizumi, Kazunori Shimazaki, Chiharu Morioka, Katsuyasu Kawano and T. Ohshima, "Degradation modeling of InGaP/GaAs/Ge triple-junction solar cells irradiated with various-energy protons," *Sol. Energy Mater. Sol. Cells*, vol. 93, no. 6–7, pp. 768–773, 2009.

[74] F. Bouzid, L. Dehimi, F. Pezzimenti, M. Hadjab, and A. H. Larbi, "Numerical simulation study of a high efficient AlGaN-based ultraviolet photodetector," *Superlattices Microstruct.*, vol. 122, pp. 57–73, 2018.

[75] O. Terghini, L. Dehimi, A. Mefteh, and H. Bencherif, "Performance evaluation and comparison of monolithic and mechanically stacked dual tandem InGaP/GaAs heterojunction on Ge Cell: A TCAD study," *Trans. Electr. Electron. Mater.*, vol. 21, no. 4, pp. 384–393, 2020.

[76] P. Michalopoulos, "A novel approach for the development and optimization of state-of-the-art photovoltaic devices using Silvaco," naval postgraduate school monterey CA, 2002.

[77] G. Verma, Manish and Routray, Soumya R and Mishra, "Analysis and optimization of BSF layer for highly efficient GaInP single junction solar cell," *Mater. Today Proc.*, vol. 43, pp. 3420–3423, 2021.

[78] R. Bernal-Correa, S. Torres-Jaramillo, and A. Morales-Acevedo, "Design of two and four-terminals InGaP/GaAs//Si tandem solar cells," in *IEEE 46th Photovoltaic Specialists Conference (PVSC)*, 2019, p. 989.

[79] C. Peng, F. Ding, Z. Lei, Z. Zhang, Y. En, and Y. Huang,

"Investigation of radiation-induced degradations in four-junction solar cell by experiment and simulation," *Microelectron. Reliab.*, vol. 108, p. 113646, 2020.

[80] G. Djaafar, F and Hadri, B and Bachir, "The Effect of a Back Surface Field (BSF) on the Efficiency of Dual Junction InGaP/GaAs Cell," 2017.

[81] K. Attari, L. Amhaimar, A. Asselman, M. Bassou, and O. And, "The design and optimization of GaAs single solar cells using the genetic algorithm and Silvaco ATLAS," *Int. J. Photoenergy*, vol. 2017, pp. 1–7, 2017.

[82] F. Djaafar, B. Hadri, and B. Bachir, "IV Characteristics of InGaP/GaAs Solar Cell with the presence of a Back Surface Field and a Tunnel junction," *J. Electr. Syst.*, vol. 14, no. 2, pp. 64–76, 2018.

[83] J. M. Olson and S. R. Kurtz, "Current-matched high-efficiency, multijunction monolithic solar cells," *US Patent 5,223,043*. Google Patents, 1993.

[84] F. Djaafar, B. Hadri, and G. Bachir, "Optimal parameters for performant heterojunction InGaP/GaAs solar cell," *Iinternational J. Hydrog. energy*, vol. 42, no. 13, pp. 8644–8649, 2017.

جـامعـة نينوى
كلية هندسة الالكترونيات
قسم الإلكترونيك

# محاكاة الخلية الشمسية عالية الكفاءة نوع

# (InGaP / GaAs)

مروه ماهر سالم المولى

رسالة ماجستير في هندسة الإلكترونيك

بإشراف

أ.د. خالد خليل محمد

1443 هـ

2021 م

محاكاة الخلية الشمسية عالية الكفاءة نوع (InGaP / GaAs)


رسالة تقدمت بها

مروه ماهر سالم المولى



إلى

مجلس كلية هندسة الالكترونيات ـ جامعة نينوى

وهي جزء من متطلبات نيل شهادة الماجستير

علوم في هندسة الالكترونيك

(الالكترونيك)



بإشراف

أ.د. خالد خليل محمد

بسم الله الرحمن الرحيم

قل هل يستوي الذين يعلمون والذين لا يعلمون

**صدق الله العظيم**

[ الزمر : 9]

**الخلاصة**

تركز هذه الأطروحة على تصميم ومحاكاة الخلايا الشمسية متعددة الطبقات (ترادفية) بناءً على مواد أشباه الموصلات III-V . تحتوي الخلايا الترادفية على سلسلة من تقاطعات p-n التي توفر تحسينًا في الكفاءة على الخلايا الشمسية المفردة عن طريق توليد الطاقة عبر طيف أوسع من الشمس. في هذه الأطروحة، تم تصميم ومحاكاة بنية خلية ترادفية (InGaP/GaAs).

تتكون هذه الخلية الترادفية من طبقتين، الأولى من فوسفيد الإنديوم الغاليوم (InGaP) كخلية عليا بفجوة طاقة مقدارها 1.87 الكترون فولت، والثانية هي ارسنيد الغاليوم (GaAs) كخلية سفلى بفجوة طاقة تبلغ 1.42 الكترون فولت، و تم محاكاة (GaAs) كوصلة نفق. أجريت الدراسة باستخدام برنامج المحاكاة المتخصص Silvaco Atlas الذي صمم لمحاكاة ودراسة سلوك الخلايا الشمسية ، وتم تنفيذ النمذجة العددية لتصميم هيكل الخلية الترادفية، وتم الحصول على أعلى كفاءة من خلال دراسة بعض العوامل المهمة للخلايا الشمسية مثل سمك الخلية متعددة الطبقات وتركيز المعززات وكذلك تأثير درجة الحرارة على أداء الجهاز.

يقوم برنامج Silvaco بإجراء عمليات المحاكاة وتم تحقيق النتائج في إطار الطيف AM1.5 .

لتحقيق هذا العمل:

أولاً، تم تصميم الخلية العلوية (InGaP) ثم تم تغيير الجزء المولي لمحتوى الإنديوم لضبط فجوة النطاق عند 1.87 فولت، وعند هذه القيمة، كانت أعلى كفاءة للخلية تساوي 17.15٪.

ثانياً، تم تصميم الخلية السفلية (GaAs) ووجد أن الكفاءة بعد المحاكاة بلغت 23.07٪ .

ثالثًا، تم تكديس الخليتين إحداهما فوق الأخرى وربطهما بواسطة تقاطع نفق من مادة أشباه الموصلات (GaAs).

تم تحقيق عوامل تشغيل عالية للخلية الترادفية عن طريق إضافة إنديوم ألومنيوم جاليوم فوسفيد (InAlGaP) كطبقة نافذة ذات فجوة نطاق تبلغ 2.3 الكترون فولت لتقليل إعادة التركيب السطحي للخلية العلوية وكطبقة مجال السطح الخلفي (BSF) للخليتين لتقليل تشتت حامل الشحنة، حيث وصلت كفاءة الخلية إلى 25.10٪.

لتحسين مواصفات تصميم الخلية الترادفية ، تمت دراسة السماكة لطبقة BSF للخلية السفلية ووجد من خلال النتائج أن أداء الخلية الشمسية قد تتأثر بزيادة سماكة هذه الطبقة. تم تحسين عرض طبقة BSF لإعطاء كفاءة حوالي 32.70٪ بسمك 2.1 مايكرومتر، تمت دراسة تأثير تركيز المعززات وسمك طبقة النافذة للخلية العلوية على أداء الخلية الترادفية (InGaP / GaAs). حيث تم تغيير سماكة طبقة النافذة من 0.01 ميكرومتر إلى 0.06 ميكرومتر وهذا أدى إلى زيادة في الكفاءة من 32.70٪ الى 33.59 ٪ ، كما تم تقليل كثافة المعززات لطبقة النافذة من $Na = 2 \times 10^{18}$ سم$^{-3}$ إلى $Na = 1 \times 10^{18}$ سم$^{-3}$، مما أدى إلى تحسن الكفاءة وجعلها تساوي 34.24٪. التحسين الآخر الذي تم تطبيقه على الخلية الترادفية هو تغيير مادة تقاطع نفق / GaAs GaAs إلى InGaP / GaAs ، مما أدى إلى تحسين الأداء العام للخلية ويصبح مساوياً لـ 34.39%. بعد

الحصول على التركيب الأمثل للخلية الترادفية ، تمت دراسة تأثير درجة الحرارة على التركيب الأمثل للخلية.حيث لوحظ أنه مع زيادة درجة الحرارة ، تنخفض كفاءة الخلية الترادفية عند 300 كلفن الى 400 كلفن بزيادات تبلغ حوالي 25 درجة.